



저작자표시-비영리-변경금지 2.0 대한민국

이용자는 아래의 조건을 따르는 경우에 한하여 자유롭게

- 이 저작물을 복제, 배포, 전송, 전시, 공연 및 방송할 수 있습니다.

다음과 같은 조건을 따라야 합니다:



저작자표시. 귀하는 원저작자를 표시하여야 합니다.



비영리. 귀하는 이 저작물을 영리 목적으로 이용할 수 없습니다.



변경금지. 귀하는 이 저작물을 개작, 변형 또는 가공할 수 없습니다.

- 귀하는, 이 저작물의 재이용이나 배포의 경우, 이 저작물에 적용된 이용허락조건을 명확하게 나타내어야 합니다.
- 저작권자로부터 별도의 허가를 받으면 이러한 조건들은 적용되지 않습니다.

저작권법에 따른 이용자의 권리는 위의 내용에 의하여 영향을 받지 않습니다.

이것은 [이용허락규약\(Legal Code\)](#)을 이해하기 쉽게 요약한 것입니다.

[Disclaimer](#)

UV-cured Solid-State Composite Polymer Electrolytes for Flexible/Safer Lithium-Ion Batteries

Se-Hee Kim

Department of Energy Engineering
(Battery Science and Technology)

Graduate school of UNIST

2015

UV-cured Solid-State Composite Polymer Electrolytes for Flexible/Safer Lithium-Ion Batteries

Se-Hee Kim

Department of Energy Engineering
(Battery Science and Technology)

Graduate school of UNIST

UV-cured Solid-State Composite Polymer Electrolytes for Flexible/Safer Lithium-Ion Batteries

A dissertation
submitted to the Graduate School of UNIST
in partial fulfillment of the
requirements for the degree of
Master of Science.

Se-Hee Kim

12. 12. 2014 of submission

Approved by



Advisor

Sang-Young Lee

UV-cured Solid-State Composite Polymer Electrolytes for Flexible/Safer Lithium-Ion Batteries

Se-Hee Kim

This certifies that the dissertation of Se-Hee Kim is approved.

12. 12. 2014 of submission



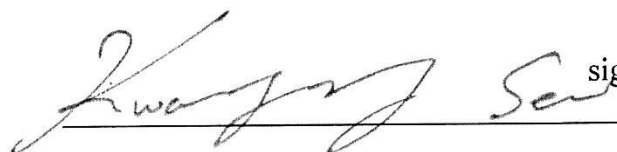
signature

Advisor: Sang-Young Lee



signature

Soojin Park



signature

Kwanyong Seo

Contents

Abstract	7
List of Figures	8
CHAPTER I. INTRODUCTION	11
CHAPTER II. MECHANICALLY COMPLIANT AND LITHIUM DENDRITE GROWTH-SUPPRESSING COMPOSITE POLYMER ELECTROLYTE	
2.1. Introduction	14
2.2. Experimental	16
2.2.1. Fabrication of composite polymer electrolyte	16
2.2.2. Characterization of composite polymer electrolyte	17
2.3. Results and discussion	18
2.3.1. The microstructure of the composite polymer electrolyte	18
2.3.2. Mechanical bendability / Electrochemical performance	20
2.3.3. Lithium-dendrite test	24
2.3.4. Cell performance	28
2.4. Conclusion	31
CHAPTER III. A SHAPE-DEFORMABLE AND SAFETY REINFORCED SOLID-STATE PLASTIC CRYSTAL COMPOSITE POLYMER ELECTROLYTE	
3.1 Introduction	32
3.2. Experimental	33
3.2.1. Fabrication of the plastic crystal composite polymer electrolyte	33
3.2.2. Characterization of the plastic crystal composite polymer electrolyte	35
3.3. Results and discussion	37

3.3.1. Structural/electrochemical uniqueness of plastic crystal composite polymer electrolyte	37
3.3.2. Electrochemical performance	44
3.3.3. Cell performance	47
3.3.4. Thermal stability	50
3.4. Conclusion	54
References	55

Abstract

Lithium-ion batteries (LIBs), as a compelling portable power source, have dominated the portable device market due to their high energy density, high voltage window and long cyclability. Flexible LIBs have received great attention as a key component to enable future flexible electronic devices as roll-up displays, touch screens, conformable active radio-frequency identification tags, wearable sensors and implantable medical devices. A number of designs for flexible LIBs have been reported in recent years.

In this study, a new class of UV (ultraviolet)-cured mechanically-compliant, dendrite growth-suppressing and thermally-stable composite polymer electrolytes (CPEs) are developed for use in flexible LIBs. These new CPEs are fabricated through an elaborate combination of UV-cured ethoxylated trimethylolpropane triacrylate macromer (serving as a mechanical framework) and Al_2O_3 nanoparticles (as a functional filler) under the presence of liquid electrolyte (1M LiPF_6 in ethylene carbonate/propylene carbonate = 1/1 v/v or succinonitrile-mediated plastic crystal electrolyte (PCE)).

A salient structural feature of the CPE is close-packed Al_2O_3 nanoparticles in the liquid electrolyte-swollen ETPTA macromer matrix. Owing to this unique morphology, the CPE provides significant improvements in the mechanical bendability and suppression of lithium dendrite growth during repeated charge/discharge cycling of cells.

In addition, the CPE precursor mixture (i.e., prior to UV irradiation) with well-tailored rheological properties, via collaboration with UV-assisted imprint lithography technique, enables the generation of micropatterned CPE with tunable dimensions. Notably, the cell incorporating the self-standing PCE based CPE, which acts as thermally-stable electrolyte and also separator membrane, maintains stable charge/discharge behavior even after exposure to thermal shock condition (= 130 °C/0.5 h), while a control cell assembled with carbonate-based liquid electrolyte and polyethylene separator membrane loses electrochemical activity.

We envision that the material/structural concept used for the CPEs is simple and versatile, which thus holds a great deal of promise as a platform electrolyte strategy for next-generation flexible LIBs.

List of figures

Figure 1. A scheme of conventional lithium-ion battery (anode: graphite, cathode: lithium cobalt oxide, and a liquid electrolyte containing lithium ions in a separator.)

Figure 2. (a) A scheme of UV-crosslinking-assisted fabrication process and photographs representing the mechanical bendability of CPE and GPE. (b) A FE-SEM photograph (cross-sectional) demonstrating structural uniqueness of CPE. (c) FT-IR spectra of acrylic C=C bonds ($1610 \sim 1625 \text{ cm}^{-1}$) of ETPTA monomer (before/after UV-crosslinking) in the CPE and GPE.

Figure 3. Mechanical bending test of: (a) CPE vs. GPE (b) Temperature-dependent ionic conductivity of GPE and CPE.

Figure 4. Mechanical bending after 1st cycle: (a) CPE; (b) GPE.

Figure 5. Linear sweep voltammograms of CPE and GPE on a working electrode of stainless-steel and a counter and reference electrode of lithium metal.

Figure 6. (a) Voltage profiles of a symmetric cell (Li metal/CPE (or GPE)/Li metal) as a function of cycle number. (b) Schematic illustrations explaining the advantageous effect of the CPE on the suppression of lithium dendrite growth. (c) A FE-SEM photograph (cross-sectional) of CPE and GPE after the repeated cycling.

Figure 7. FE-SEM photographs (surface) of: (a) CPE; (b) GPE after the repeated cycling.

Figure 8. Discharge profiles of cells as a function of discharge current density (from 0.1 C to 1.0 C) at a constant charge current density of 0.1 C: (a) CPE; (b) GPE. (c) Charge/discharge profiles of cells assembled with CPE (or GPE) as a function of cycle number (= cycling performance) at a constant charge/discharge current density of 0.5 C/0.5 C. (c) Comparison of cycling performance between CPE and GPE.

Figure 9. Variation in AC impedance spectra (1st \rightarrow 50th cycle) of cells assembled with: (a) CPE; (b) GPE.

Figure 10. A schematic representation of UV curing-assisted fabrication process for PC-CPE, wherein chemical structures and photographs depicting mechanical bendability of PC-CPE are also depicted.

Figure 11. Structural characterization of PC-CPE: (a) DSC profiles showing characteristic transition temperatures (T_{cp} and T_m) of SN in PCE and PC-CPE; (b) FT-IR spectra (before/after UV curing) of acrylic C=C bonds ($1610 \sim 1625 \text{ cm}^{-1}$) of ETPTA in PC-CPE; (c) cross-sectional FE-SEM images of PC-CPE (thickness $\sim 110 \mu\text{m}$), wherein the high-magnification view exhibits the presence of highly-reticulated interstitial voids (that are originally occupied with PCE) formed between the Al_2O_3 nanoparticles.

Figure 12. Mechanical flexibility of PC-CPE: (a) comparison of bendability between PC-CPE and control solid-state electrolyte incorporating no Al_2O_3 nanoparticles, wherein the samples are subjected to repeated bending cycle at a strain rate of 10 mm min^{-1} under longitudinal strain ranging from 1 to 3 cm; (b) photographs of PC-CPE after being wound along a glass rod (diameter = 2.5 and 5 mm), wherein the inset shows that neither micro-scale cracks nor physical defects are formed.

Figure 13. Rheological behavior of PC-CPE and carbonate-based liquid electrolyte (1M LiPF_6 in EC/DMC = 1/1 v/v), wherein viscosity is plotted as a function of shear rate.

Figure 14. Structural characterization of maze-patterned PC-CPE: (a) a schematic illustration of UV-IL technique-driven micropatterning procedure; (b) OM image of PC-CPE precursor mixture prior to UV exposure; (c) FE-SEM image (top view) of microscale maze-patterned PC-CPE; (d) FE-SEM image (cross-sectional view) of microscale maze-patterned PC-CPE, wherein the inset shows that Al_2O_3 nanoparticles are closely packed in the micropatterned PC-CPE.

Figure 15. Temperature-dependent ionic conductivity (temperature range = $30 - 70 \text{ }^\circ\text{C}$) of PC-CPE and carbonate-based liquid electrolyte (1M LiPF_6 in EC/DMC = 1/1 v/v).

Figure 16. Linear sweep voltammograms (LSV) of PC-CPE at a scan rate of 1.0 mV s^{-1} .

Figure 17. Charge/discharge profiles of coin-type full cells as a function of cycle number, wherein the cells are cycled at a constant charge/discharge current density of 0.2 C ($= 0.40 \text{ mA cm}^{-2}$)/ 0.2 C under a voltage range of 1.5 - 2.7 V: (a) $\text{LiCoO}_2/\text{PC-CPE}/\text{Li}_4\text{Ti}_5\text{O}_{12}$; (b) $\text{LiCoO}_2/\text{PE separator}/\text{Li}_4\text{Ti}_5\text{O}_{12}$.

Figure 18. Variation in AC impedance spectra ($1^{\text{st}} \rightarrow 40^{\text{th}}$ cycle) of cells assembled with PC-CPE.

Figure 19. Thermal stability of Al pouch-type full cells assembled with PC-CPE or carbonate-based liquid electrolyte (1M LiPF₆ in EC/DMC = 1/1 v/v) and PE separator: (a) variation in charge/discharge profiles of cells after exposure to thermal shock (= 130 °C/0.5 h); (b) variation in discharge capacity and charge voltage (inset) of cells before/after the thermal shock. (c) Comparison of thermal shrinkage between PC-CPE and PE separator after exposure to the thermal shock. (d) Ionic conductivity of PC-CPE before/after the thermal shock.

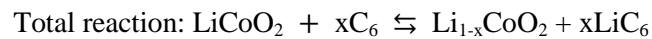
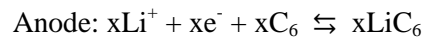
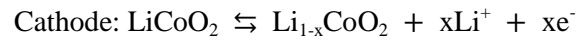
Figure 20. Variation in AC impedance spectra of cells assembled with PC-CPE after exposure to thermal shock (= 130 °C/0.5 h).

Figure 21. (a) Photographs showing the swelling behavior of cells assembled with PC-CPE or carbonate-based liquid electrolyte (1M LiPF₆ in EC/DMC = 1/1 v/v), after exposure to thermal shock (= 130 °C/0.5 h). (b) Dynamic mode TGA profiles of PC-CPE and carbonate-based electrolyte (1M LiPF₆ in EC/DMC = 1/1 v/v).

CHAPTER I. INTRODUCTION

Lithium-ion batteries (LIBs), as the main power source, dominate the portable device market due to their high energy density, high voltage window, long cyclability and eco-friendly operation.¹

Rechargeable LIBs based on the intercalation concept were first suggested by Armand in 1972. A conventional LIB consists of a carbon anode and a lithium metal oxide cathode with a polymer separator, an organic liquid electrolyte of lithium salt with an organic solvent mixture and metal foil or mesh current collector (Fig. 1). In the LIBs, the lithium ions are passes through the separator in electrolyte from the cathodes to the anodes during charging state while the electrons move from the cathodes to the anodes through the external circuit. The discharge reaction is a reverse reaction of the above reaction. The equations of chemical reactions during the charge/discharge are as follows. The LiCoO_2 as cathode and graphite as anode have been used in equation.



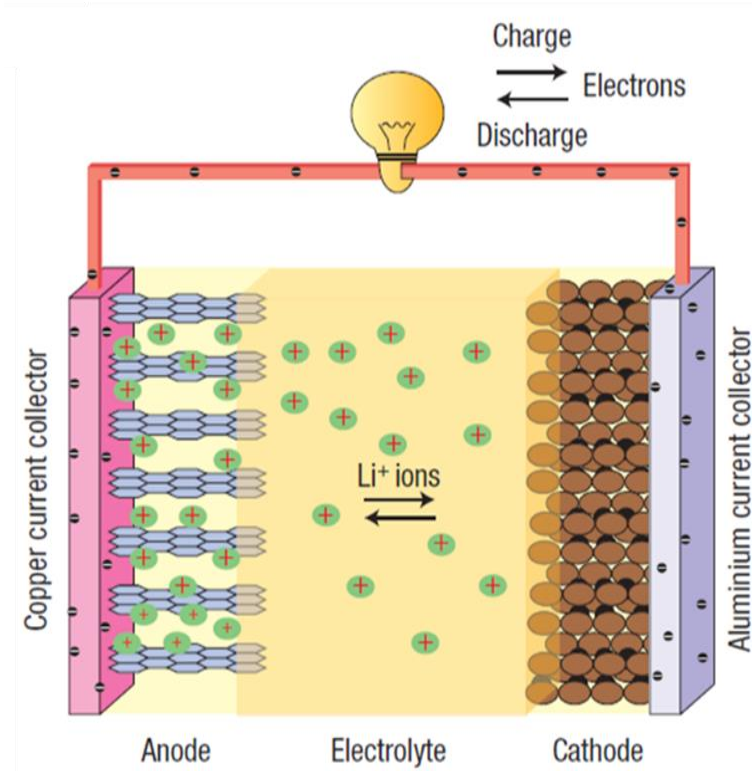


Figure 1. A scheme of conventional lithium-ion battery (anode: graphite, cathode: lithium cobalt oxide, and a liquid electrolyte containing lithium ions in a separator.)

Rapidly emerging flexible/wearable electronic devices with unusual shape diversity and mobile usability, including wrist-mounted cellular phones, roll-up displays, Google Glass, smart electronic clothing (so-called “e-textiles”), wearable robotic suits and implantable/patchable sensors, draw considerable attention as a kind of disruptive technology to drastically change our daily lives.^{2,3} Stimulated by such promising prospect, a number of global electronics makers are fiercely competing to preoccupy this attractive market. To accelerate the advent of the smart electronics era, along with never-ceasing pursuit of high-performance flexible displays and memory chips, development of thin, lightweight and flexible rechargeable power sources should be indispensably required.

Among various rechargeable energy storage systems, current state-of-the art lithium-ion batteries, the most widespread portable power source, could be suggested as a promising solution to fulfill the stringent requirements for flexible electronics.⁴⁻⁸ From the cell manufacturing point of view, conventional lithium-ion batteries with fixed shapes and sizes are generally fabricated by winding (or stacking) cell components (such as anodes, cathodes and microporous separator membranes) and then packaging them with (cylindrical-/rectangular-shaped) metallic canisters or pouch films, finally followed by injection of liquid electrolytes. In particular, the use of liquid electrolytes gives rise to serious concerns in cell assembly, because they require strict packaging materials to avoid leakage problems and also separator membranes to prevent electrical contact between electrodes.^{4,6,9} For these reasons, the conventional cell assembly and materials have pushed the batteries to lack of variety in form factors, thus imposing formidable challenges on their integration into versatile-shaped electronic devices.

The abovementioned design limitation of traditional batteries has spurred us to pay much attention to flexible batteries with shape/design diversity. To date, many of the research works on flexible batteries have been primarily devoted to rational design/synthesis/structural engineering of electrode materials. Details on the previous studies have been comprehensively described in the review articles.⁶⁻¹⁰ Some representative achievements include the nanostructured electrode materials based on low-dimensional carbon materials such as carbon nanotube and graphene, and also 3-dimensional (3D) non-metallic current collectors exploiting conductive/compliant papers and textiles.¹¹⁻¹⁵ Meanwhile, to replace combustible and fluidic liquid electrolytes, which are believed to be a major threat to cell safety and electrolyte leakage failures, solid-state (in particular, polymer-mediated) electrolytes with balanced electrochemical properties and mechanical flexibility have been demonstrated.^{5,16,17}

CHAPTER II. MECHANICALLY COMPLIANT AND LITHIUM DENDRITE GROWTH-SUPPRESSING COMPOSITE POLYMER ELECTROLYTE

2.1. Introduction

Rapid growth of next-generation portable electronic devices with aesthetic diversity and unique functionality, including smart mobile gadgets, wearable/patchable electronic systems, roll-up displays, and implantable medical devices, has accelerated the development of flexible lithium-ion batteries as a suitable power source. As previously mentioned, commercial lithium-ion batteries consist of cathodes, anodes, liquid electrolytes, and polyolefin separator membranes.

Among these major components of cells, the use of liquid electrolytes poses a serious obstacle to varying cell design. This formidable challenge strongly stimulates research activities in exploring polymer electrolytes with mechanical compliance and robust safety features, which thus can offer a wide range of form factors and allow facile integration into cells of different sizes and shapes.¹⁸⁻²⁰ Among a wide variety of polymer electrolyte candidates investigated so far, gel polymer electrolytes (GPEs), which are generally composed of polymer matrices and liquid electrolytes, have garnered considerable attention owing to their unique so matter characteristics such as good ionic conductivity, self-standing capability and electrolyte leakage-proof.^{21,22} The GPEs, however, suffer from a trade-off issue between mechanical properties and ionic conductivity. Our group^{16,23,24} has recently reported a new strategy to fabricating mechanically strong GPEs without impairing their electrochemical performance. A key factor for synthesis of the GPEs was the introduction of UV-cured ethoxylated trimethylolpropane triacrylate (ETPTA) macromere bearing trivalent vinyl groups as an effective mechanical framework.^{16,24,25} Meanwhile, a new composite polymer electrolyte, including inorganic nanoparticles in addition to the crosslinked ETPTA macromer, was also reported in our previous study.²⁶ Unusual physicochemical characteristics (in particular, imprintability and facile integration with 3D-structured electrodes) of the composite polymer electrolyte were comprehensively explored.

In this part, as a part of ongoing research efforts to develop advanced polymer electrolytes, we demonstrate mechanically compliant and lithium dendrite growth-suppressing composite polymer electrolytes for use in flexible lithium ion-batteries. Especially, the lithium dendrite growth between electrodes is considered a major cause of internal short-circuit problems of cells, which are believed to be one of the most critical hazards to battery safety.^{18-20,22} Therefore, the role of polymer electrolytes as a separator (maintaining electrical isolation between the electrodes) becomes important in the development of flexible batteries. The composite polymer electrolyte (hereinafter, referred to as “CPE”) proposed herein is fabricated by finely combining a UV-cured ETPTA macromer with alumina (Al_2O_3) nanoparticles in the presence of a high boiling point liquid electrolyte (1M LiPF_6 in

ethylene carbonate (EC)/propylene carbonate (PC) = 1/1 v/v, boiling point > 200 °C). The Al₂O₃ nanoparticles are integrated as a functional filler to improve mechanical properties, interfacial stability toward electrodes, and cell safety (here, suppression of lithium dendrite growth that causes internal short-circuit failure during charge–discharge cycling).

An unusual structural feature of the CPE is the formation of densely packed Al₂O₃ nanoparticles in the liquid electrolyte swollen ETPTA macromer matrix. The CPE with this unique microstructure is expected to show considerable improvements in solid electrolyte properties (specifically, mechanical bendability and suppression of lithium dendrite growth during cycling), as compared to a control GPE incorporating no Al₂O₃ nanoparticles.

2.2. Experimental

2.2.1. Fabrication of composite polymer electrolyte

The precursor solution (i.e., before UV-curing) of CPE was prepared by mixing vacuum-dried Al_2O_3 nanoparticles (average particle size = 300 nm) with ETPTA ($M_w = 428$, trivalent acrylate monomer) and 2-hydroxy-2-methyl-1-phenyl-1 propanon (HMPP, photo-initiator) in the presence of a liquid electrolyte (1 M LiPF_6 in EC/PC = 1/1 v/v, Soulbrain). The weight-based composition ratio of the precursor solution was (liquid electrolyte/ETPTA = 85/15 w/w)/ Al_2O_3 = 30/70 w/w, wherein the concentration of HMPP was fixed at 1.0 wt% of the ETPTA content. The precursor solution was then mixed via bead-milling for 0.5 h, in order to secure uniform dispersion of Al_2O_3 nanoparticles. Thereafter, the precursor solution was cast onto a poly(ethylene terephthalate) (PET) sheet and then exposed to UV-irradiation for 20 s, resulting in the formation of a solidified, self-standing CPE film. The UV-crosslinking was performed using a Hg UV-lamp (Lichtzen), with an irradiation peak intensity of approximately 2000 mW cm^{-2} on the sample surface.^{16,23,24} The thickness of the resulting CPE film was approximately 150 μm . Meanwhile, the GPE, as a control sample, was fabricated by adopting the same materials, compositions, and procedure as ones used for the CPE, but excluding Al_2O_3 nanoparticles. A schematic representation illustrating the UV-irradiation-assisted fabrication process and a photograph depicting mechanical bendability of the CPE are provided in Fig. 2(a).

2.2.2. Characterization of microstructure, mechanical bendability, and electrochemical performance of composite polymer electrolyte

The UV-crosslinking reaction of the ETPTA macromer in the CPE was elucidated using a FT-IR spectrometer (FT-3000, Excalibur).^{16,24-27} The gel content of CPE was determined by measuring the weight loss of samples after solvent extraction using dimethyl carbonate (DMC) at 70 °C for 8 h and subsequently acetone at room temperature for 24 h.^{16,24} The dispersion state of Al₂O₃ nanoparticles in the CPE was characterized using a field emission scanning electron microscope (FE-SEM, S-4300, Hitachi). The mechanical bendability of CPE was measured using a universal tensile tester (Lloyd LR 10K, Lloyd Instruments), where samples were subjected to repeated bending stress until they mechanically ruptured at a strain rate of 10 mm min⁻¹. The number of bending cycles before breakdown of the samples quantitatively represents their mechanical bendability.^{16,23} The ionic conductivity of CPE was obtained with an impedance analyzer (VSP classic, Bio-Logic) over a frequency range of 1 to 10⁶ Hz in a temperature range of 30 to 80 °C. The electrochemical tolerance of CPE against internal short-circuit failure (i.e., lithium dendrite growth between electrodes) of cells was evaluated by measuring time evolution of voltage for a symmetrical cell (Li metal/CPE/Li metal, 2032-type coin) during repeated charge–discharge reactions,²⁸⁻³⁰ where the cell was cycled under a constant current mode (CC, charge–discharge current density = 0.25 mA cm⁻²) for 0.5 h until an abrupt change in voltage profiles was detected. The charge–discharge behavior of cells was investigated using battery test equipment (PNE Solution). For evaluation of cell performance, a unit cell (2032-type coin) was assembled by sandwiching a self-standing CPE between a Li metal anode and a liquid electrolyte (1 M LiPF₆ in EC/PC = 1/1 v/v)-soaked LiCoO₂ cathode (LiCoO₂ (KD10, Umicore)/PVdF/Super-P = 95/3/2 w/w/w). The discharge current densities were varied from 0.1 (= 0.11 mA cm⁻²) to 1.0 C at a constant charge current density of 0.1 C in a voltage range between 3.0 and 4.2 V. The cells were cycled at a constant charge–discharge current density of 0.5 C/0.5 C.

2.3. Results and discussion

2.3.1. The microstructure of the composite polymer electrolyte

The microstructure (specifically, the dispersion state of Al₂O₃ nanoparticles and the chemical structure of the UV-cured ETPTA macromer skeleton) of the CPE was characterized. A FESEM image (Fig. 2(b), cross-sectional view) shows that the Al₂O₃ nanoparticles are uniformly dispersed and also densely packed in the CPE. This is attributed to the relatively large content of Al₂O₃ nanoparticles over other components (Al₂O₃ nanoparticles/liquid electrolyte swollen ETPTA macromer = 70/30 w/w) and also a good compatibility between the Al₂O₃ nanoparticles and the ETPTA macromer. Here, it should be noted that this unique morphology of the CPE is expected to play a key role in providing significant improvements in mechanical bendability and suppression of lithium dendrite growth during cycling, which will be further discussed below.

Because the abovementioned FE-SEM measurement should be conducted in a vacuum state, the liquid electrolyte swollen in the ETPTA macromer matrix was pre-removed using dimethyl carbonate (as an etching solvent). Thus, the large numbers of interstitial voids formed between the Al₂O₃ nanoparticles (Fig. 2(b)) represent the original spaces occupied by the liquid electrolyte. This porous structure demonstrates the successful evolution of highly continuous, ion-conductive network channels in the CPE, which in turn contributes to imparting facile ion transport.

The UV-crosslinking reaction of the ETPTA macromer skeleton in the CPE was examined by carrying out FT-IR analysis, where the change in the FT-IR peaks (before/after UV-irradiation) assigned to acrylic C=C bonds (1610–1625 cm⁻¹)^{16,24-27} of the ETPTA monomer was monitored. Fig. 2(c) shows that, after the UV-crosslinking, the FT-IR peaks of C=C bonds in the CPE disappear. Meanwhile, the FT-IR peaks of the GPE as a control sample was also characterized. No significant difference in the FT-IR peaks of acrylic C=C bonds was observed between the CPE and the GPE, verifying that the ETPTA monomer is successfully photo-polymerized even in the presence of Al₂O₃ nanoparticles. This can be further confirmed by measuring the gel content of the CPE. The gel content (i.e., insoluble polymer fraction after solvent (dimethyl carbonate followed by acetone) extraction^{16,24}) of the CPE was found to be more than 99% by weight (herein, the weight of Al₂O₃ nanoparticles are excluded for this measurement). This result demonstrates that the UV-crosslinking reaction of the ETPTA monomer is almost completed.

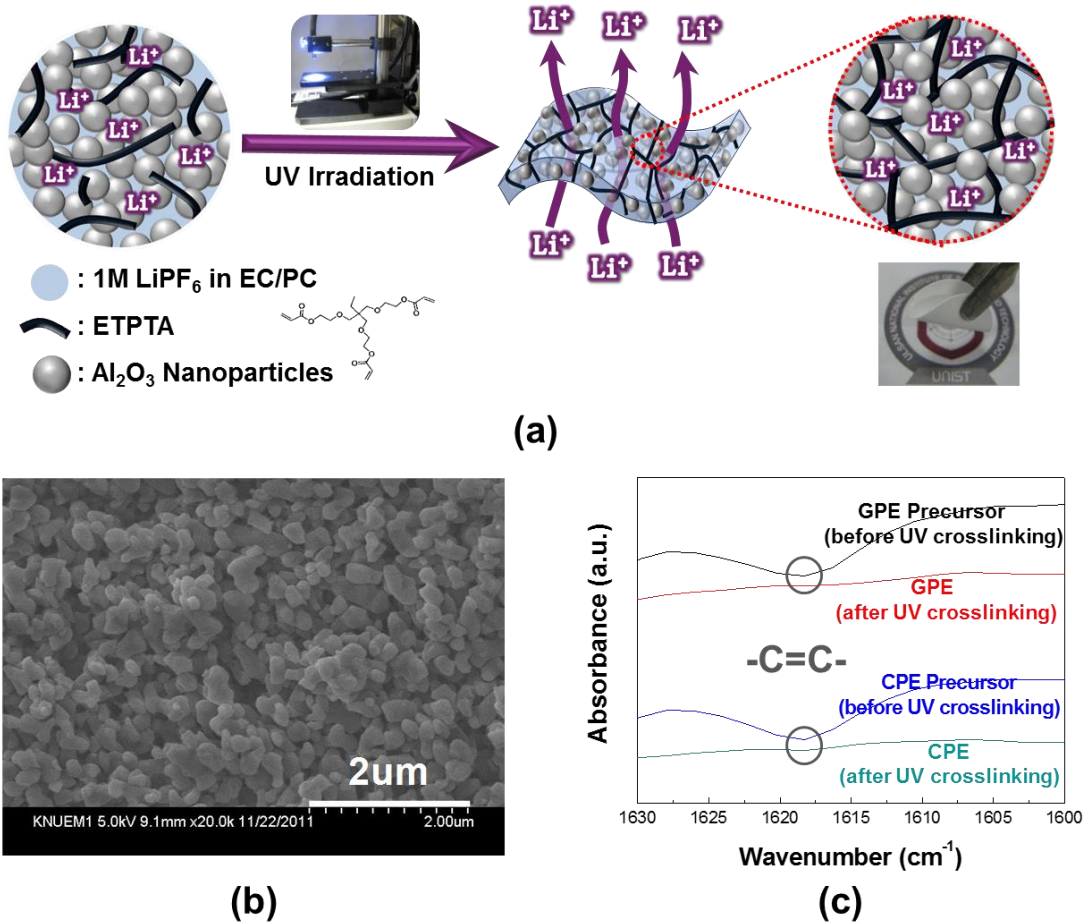


Figure 2. (a) Schematic representations illustrating UV-crosslinking-assisted fabrication process and photographs depicting the mechanical bendability of CPE and GPE. (b) A FE-SEM photograph (cross-sectional) demonstrating structural uniqueness of CPE. (c) FT-IR spectra of acrylic C=C bonds (1610 ~ 1625 cm^{-1}) of ETPTA monomer (before/after UV-crosslinking) in the CPE and GPE.

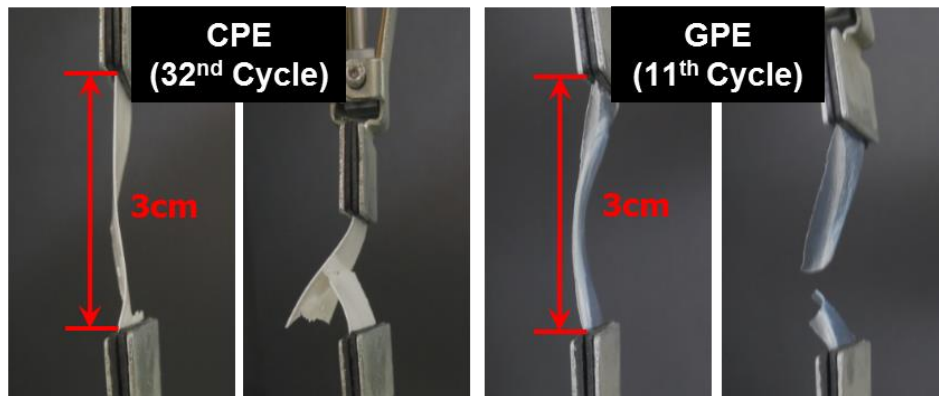
2.3.2. Mechanical bendability / Electrochemical performance

The mechanical bendability of the CPE was quantitatively investigated using a bending test and compared with that of the GPE (Fig. 3(a)). Both the CPE and GPE exhibit strong resistance to mechanical breakage upon appreciable bending stress (Fig. 4), despite a low concentration of the ETPTA macromer (ETPTA macromer/liquid electrolyte = 15/85 w/w). This underlines that the UV-crosslinked ETPTA macromere skeleton employed herein is effective in securing the mechanical bendability of the CPE and GPE.

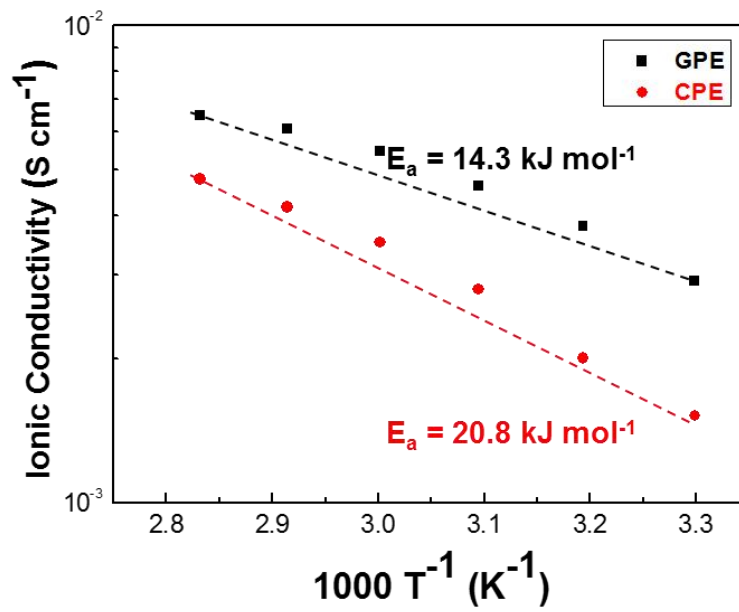
A noteworthy finding is that the CPE preserves its dimensional stability until the 32nd bending cycle (left-side image of Fig. 3(a)), whereas the GPE is broken down after the 11th bending cycle (right-side image of Fig. 3(a)). A plausible speculation on this intriguing behavior is that the well-dispersed, close-packed Al₂O₃ nanoparticles in the CPE may serve as a mechanical buffer to decentralize the stress build-up arising from repeated bending strain. It has been already reported that, in conventional nanocomposites, the presence of well-dispersed inorganic nanoparticles in a polymer matrix beneficially contributes to improving mechanical toughness of the nanocomposites, owing to the evolution of micro-voids that deconcentrate the external stress exerted on the nanocomposites.³¹⁻³³

The temperature-dependent ionic conductivity of the CPE was examined and compared with that of the GPE. Fig. 3(b) shows that, due to the high concentration of the liquid electrolyte (liquid electrolyte/ETPTA macromer = 15/85 w/w) and also highly developed ion-conductive network channels, the CPE provides satisfactory ionic conductivities of more than 10⁻³ S cm⁻¹ at room temperature. Meanwhile, over a wide range of temperatures, the ionic conductivity of the CPE is observed to be slightly lower than that of the GPE. This difference in the ionic conductivity between the GPE and the CPE can be explained by considering a tortuous path^{34,35} of ionic movement. In comparison to the GPE, a considerable amount of Al₂O₃ nanoparticles (Al₂O₃ nanoparticles/liquid electrolyte swollen ETPTA macromer = 70/30 w/w) is incorporated in the CPE. This implies that the ionically inert Al₂O₃ nanoparticles may cause an increase in tortuous path for ionic transport, behaving as a kind of obstacle to ionic migration. This relatively inactive ionic movement of the CPE is further confirmed by the slightly higher activation energy of ionic conduction⁸ (E_a = 20.8 kJ mol⁻¹ for CPE vs. 14.3 kJ mol⁻¹ for GPE).

The electrochemical stability window of the CPE and also GPE was estimated from linear sweep voltammograms (Fig. 5). No decomposition of any components in the CPE as well as GPE takes place below 4.5 V vs. Li⁺/Li. This demonstrates that, similar to the GPE, the CPE presents a high anodic stability and thus could be potentially applied to high-voltage lithium-ion batteries.

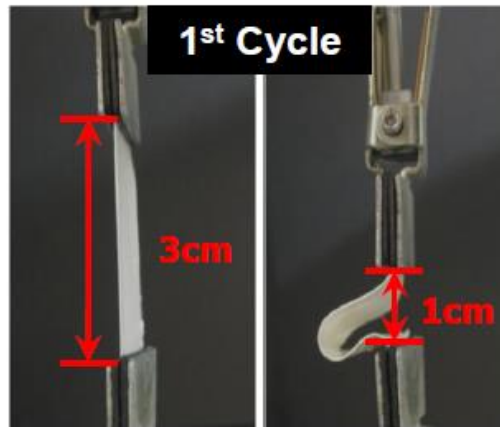


(a)

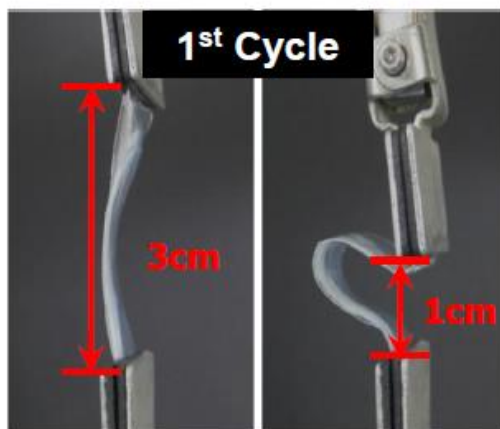


(b)

Figure 3. Mechanical bending test of: (a) CPE vs. GPE (b) Temperature-dependent ionic conductivity of GPE and CPE.



(a)



(b)

Figure 4. Mechanical bending after 1st cycle: (a) CPE; (b) GPE.

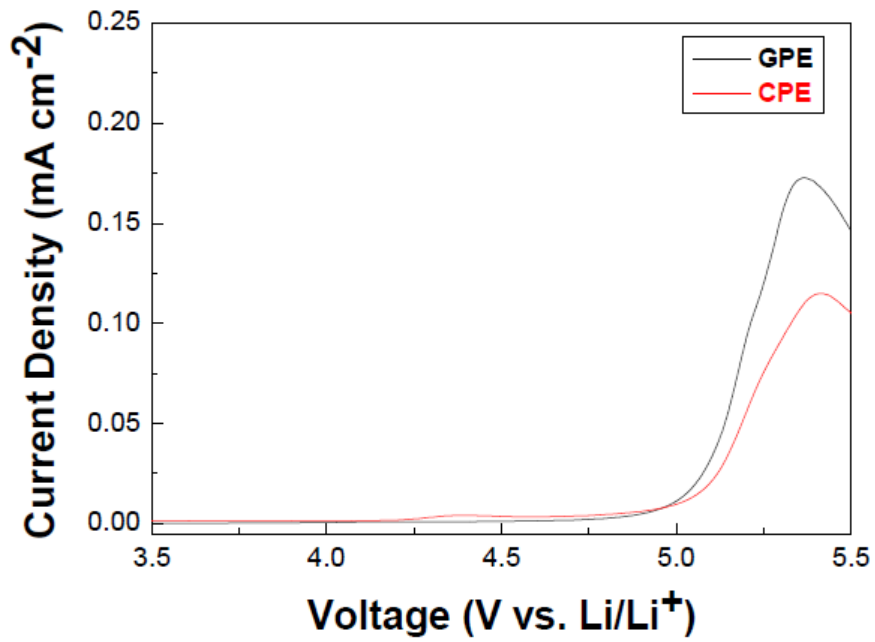


Figure 5. Linear sweep voltammograms of CPE and GPE on a working electrode of stainless-steel and a counter and reference electrode of lithium metal.

2.3.3. Lithium-dendrite test

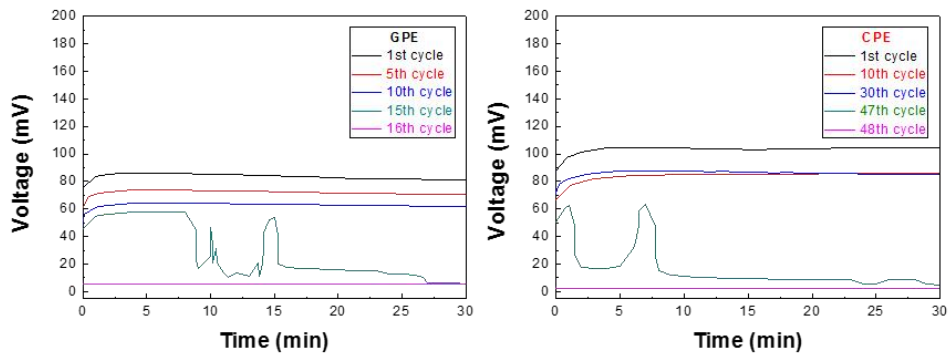
When polymer electrolytes are assembled into lithium-ion batteries, they should act as an ion-conductive electrolyte and also a separator preventing electrical contact between an anode and a cathode. In particular, while addressing internal short-circuit problems (mainly arising from lithium dendrite growth between electrodes) of cells, the role of polymer electrolytes as a separator becomes more important. Here, in order to examine the effect of the CPE on the suppression of internal short-circuit failure, a symmetric cell, which is composed of Li metal/CPE/Li metal, was prepared based on experimental schemes reported in previous publications.²⁸⁻³⁰ In this measurement, time evolution of cell voltage during repeated charge–discharge cycling was monitored. An abrupt change in voltage profiles during cycling indicates the occurrence of internal short-circuit of a cell, indicating that lithium dendrites sufficiently grow and finally reach the counter electrode after penetrating through a polymer electrolyte.

Fig. 6(a) shows the charge profiles of cells assembled with the CPE (or GPE) as a function cycle number. When the symmetric cell is charged, a potential difference (i.e., voltage) between the lithium metal electrodes is generated and maintained in the range of 60–80 mV during the charging period.^{29,30} Meanwhile, when the cell is discharged, the cell voltage returns to an equilibrium value (= 0 V). An intriguing finding is that, in the GPE, the cell voltage sharply drops and fluctuates when it goes through the 15th cycle. Since then, the cell voltage has no longer changed and remains to be 0 V. This indicates that an internal short-circuit of the cell may occur at the 15th cycle, which is ascribed to the penetration of lithium dendrites through the GPE.

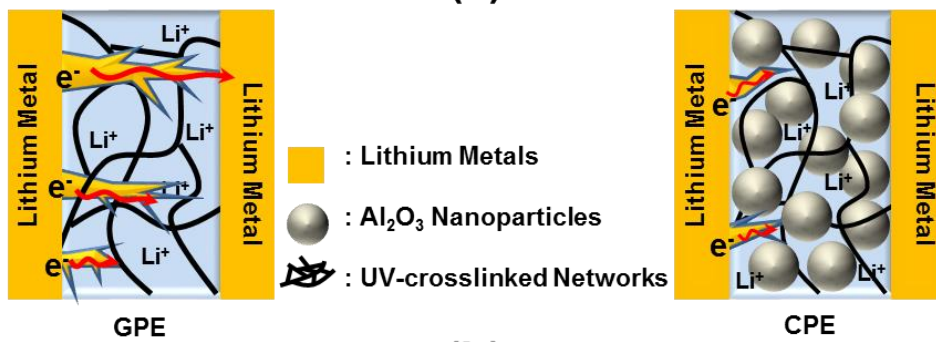
By contrast, the CPE exhibits the stable voltage profile until the 46th cycle. At the 47th cycle, the cell voltage of the CPE gets disturbed. This result demonstrates that the growth of lithium dendrites, causing the internal short-circuit failure of a cell, is substantially retarded in the CPE, owing to the presence of uniformly dispersed and densely packed Al₂O₃ nanoparticles. This beneficial effect of the CPE on the improvement of cell safety is schematically illustrated in Fig. 6(b), wherein the Al₂O₃ nanoparticles act as a protective barrier to retard growth of lithium dendrite between electrodes.

This advantageous effect of the CPE on the suppression of lithium dendrite growth was further confirmed by examining morphologies of the GPE and CPE after the repeated cycling tests. Here, the cells after the 16th cycle were chosen, where the cell voltage of the GPE drops to 0 V while the cell assembled with the CPE still shows stable charge behavior. A cross-sectional view of the GPE (left image of Fig. 6(c)) clearly shows the formation of highly developed dimples, corresponding to original spaces occupied by lithium dendrites grown during the repeated charge–discharge reactions. This facile growth of lithium dendrites in the GPE is also evidenced by observing its surface morphology (Fig. 7(a)). In comparison, no appreciable dimples or defects were detected in the CPE (right image of Fig. 6(c) and Fig. 7(b)). This morphological characterization is a good evidence to

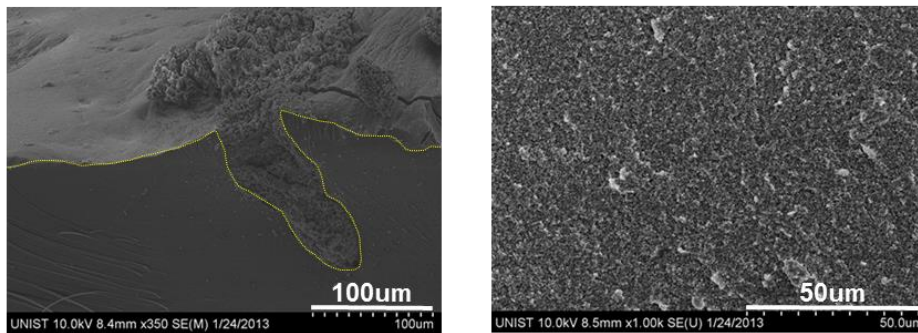
verify the superiority of the CPE over the GPE in mitigating the lithium dendrite growth during charge-discharge cycling. More importantly, it is anticipated that the CPE showing the unusual safety-reinforcement could be applied to next-generation lithium batteries (such as lithium–air and lithium–sulfur systems) adopting lithium metal as an anode.



(a)

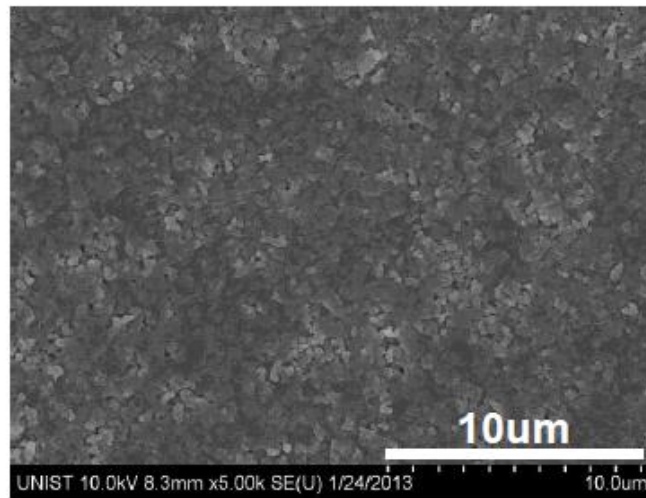


(b)

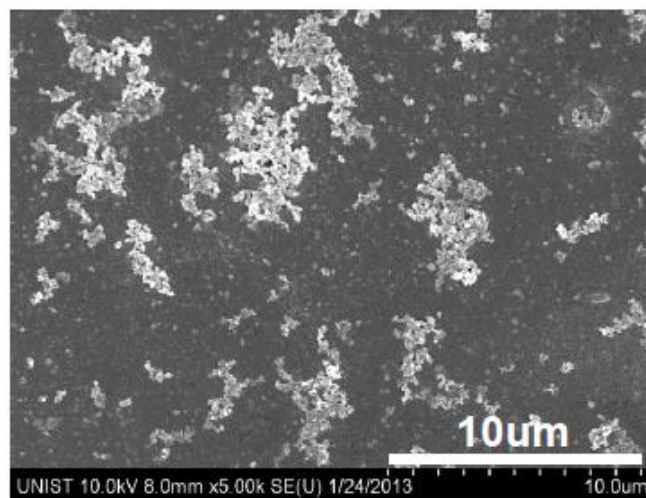


(c)

Figure 6. (a) Voltage profiles of a symmetric cell (Li metal/CPE (or GPE)/Li metal) as a function of cycle number. (b) Schematic illustrations explaining the advantageous effect of the CPE on the suppression of lithium dendrite growth. (c) A FE-SEM photograph (cross-sectional) of CPE and GPE after the repeated cycling.



(a)



(b)

Figure 7. FE-SEM photographs (surface) of: (a) CPE; (b) GPE after the repeated cycling.

2.3.4. Cell performance

The potential application of the CPE to a lithium-ion battery was explored by evaluating the cell performance. Fig. 8(a) and (b) depict discharge profiles of cells assembled with the CPE and GPE as a function of discharge current density. The cells were charged at a constant current density of 0.1 C and discharged at various current densities ranging from 0.1 to 1.0 C in a voltage range between 3.0 and 4.2 V. The initial discharge capacity (at a discharge current density = 0.1 C) of the CPE was observed to be around 138 mA h g⁻¹, which appears to be insignificantly different from that of the GPE. This clearly demonstrates that the highly continuous ion-conductive network channels are successfully established in the CPE.

The CPE (Fig. 8(a)) shows slightly lower discharge capacities than the GPE (Fig. 8(b)) at high discharge current densities where the influence of ionic transport on ohmic polarization (i.e., IR drop) is more pronounced.^{16,23,24} This inferior discharge C-rate capability of the CPE can be explained by comparing the ionic conductivity of the CPE with that of the GPE. The CPE was found to present a lower ionic conductivity (Fig. 3(b)) than the GPE due to the presence of close-packed Al₂O₃ nanoparticles. Hence, this relatively sluggish ionic transport of the CPE may give rise to escalation of the ohmic polarization of cells, leading to the loss of discharge capacities at high discharge current densities. However, it should be noted that the difference in the discharge C-rate capability between the CPE and the GPE is not appreciably large.

The cycling performance (i.e., discharge capacity of a cell as a function of cycle number) of a cell assembled with the CPE was examined (Fig. 8(c)) and also compared with that of the GPE (Fig. 8(d)). It is observed that the discharge capacity retention of the CPE (~96.2%) after the 50th cycle is comparable to that of the GPE (~95.9%). This excellent cycling performance of the CPE can be further explained by analyzing the AC impedance spectra of cells after the 1st and 50th cycle (Fig. 9). In comparison to the GPE, the growth of the cell impedance is suppressed in the CPE. This reflects the stabilized interface between the CPE and electrodes, which may be due to benign interfacial compatibility of the CPE with electrodes. Previous studies³⁶⁻³⁸ reported that the incorporation of ceramic nanoparticles into polymer electrolytes or separator membranes could contribute to alleviating growth of cell impedance, which in turn exerted a beneficial influence on cycling performance. Therefore, it may be postulated that the superior interfacial stability with electrodes, along with the well-developed ion conductive network channels, allows the CPE to provide a good cycling performance comparable to that of the GPE.

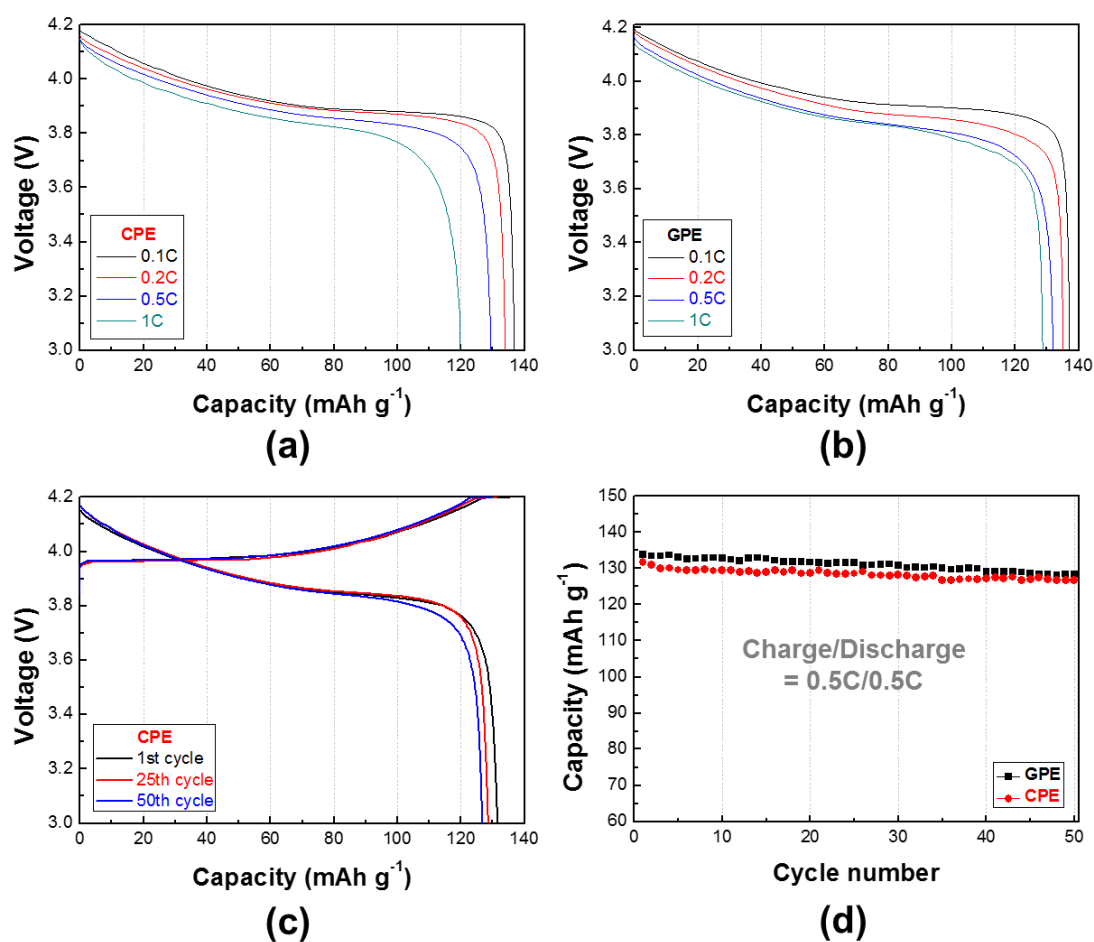


Figure 8. Discharge profiles of cells as a function of discharge current density (from 0.1 C to 1.0 C) at a constant charge current density of 0.1 C: (a) CPE; (b) GPE. (c) Charge/discharge profiles of cells assembled with CPE (or GPE) as a function of cycle number (= cycling performance) at a constant charge/discharge current density of 0.5 C/0.5 C. (d) Comparison of cycling performance between CPE

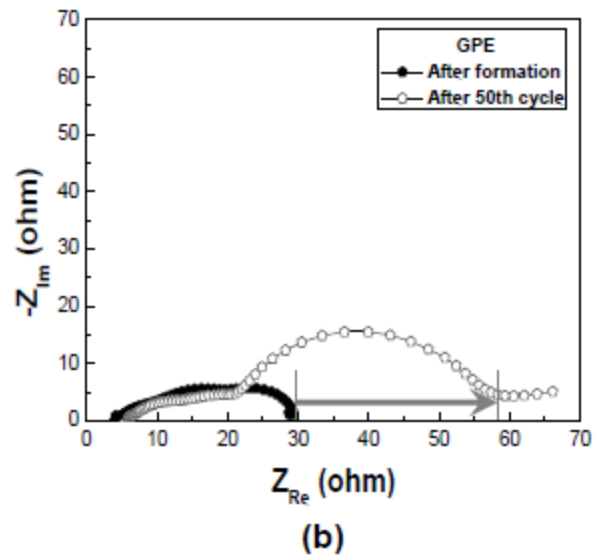
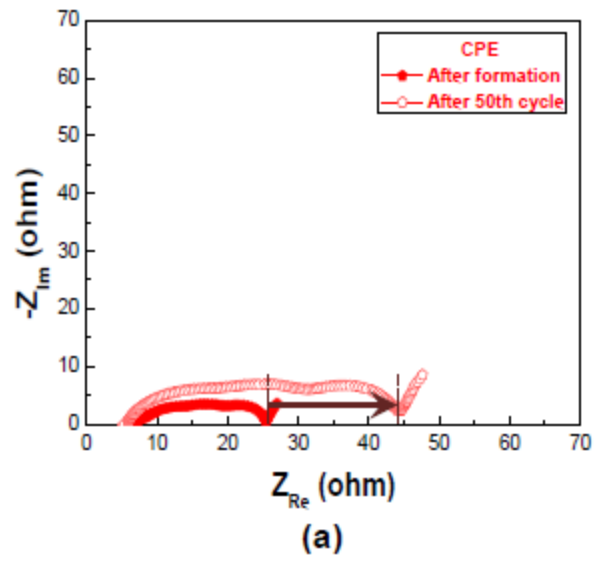


Figure 9. Variation in AC impedance spectra ($1^{st} \rightarrow 50^{th}$ cycle) of cells assembled with: (a) CPE; (b) GPE.

2.4. Conclusion

A mechanically compliant and lithium dendrite growth-suppressing composite polymer electrolyte (CPE) for use in flexible lithium-ion batteries has been demonstrated. A salient structural feature of the CPE was the uniformly dispersed, close-packed Al_2O_3 nanoparticles in the liquid electrolyte-swollen ETPTA macromer matrix. This unusual morphology of the CPE played a viable role in bringing significant improvements in the mechanical bendability and the suppression of lithium dendrite growth during the repeated charge–discharge cycling, as compared to a control GPE incorporating no Al_2O_3 nanoparticles. The benign interfacial compatibility of the CPE with electrodes, along with the well-developed ion-conductive network channels, contributed to imparting a satisfactory cycling performance comparable to that of the GPE. We believe that the CPE with the abovementioned advantageous characteristics can be suggested as a promising solid electrolyte for flexible lithium-ion batteries (in particular, struggling with formidable safety challenge).

CHAPTER III. A SHAPE-DEFORMABLE AND SAFETY REINFORCED SOLID-STATE PLASTIC CRYSTAL COMPOSITE POLYMER ELECTROLYTE

3.1. Introduction

Recently, our group reported the bendable and shape-conformable composite gel polymer electrolyte consisting of a UV-crosslinked polymer, carbonate-based liquid electrolyte and nanoparticles.^{17,26} The composite gel polymer electrolyte showed the unusual electrochemical/physical features and suppression of lithium dendrite growth. Here, as part of a continuing effort to develop advanced solid-state electrolytes for use in flexible batteries, demonstrate a new class of shape-deformable and safety reinforced solid-state electrolyte based on PC-CPE. The plastic crystal electrolyte is composed of lithium salts and a plastic crystal matrix. In this study, as a non-ionic type plastic crystal matrix, succinonitrile (SN, NC-CH₂-CH₂-CN) is chosen. The SN-mediated PCE (referred to as “PCE”) is known to provide excellent thermal stability and ionic transport owing to the high boiling point (above 200 °C) and structural defects (i.e., trans-gauche isomerism) of the plastic crystal phase that exists between the crystalline phase and the molten state.^{9,16,39-41} The PCE is combined with UV-cured ETPTA macromer/close-packed Al₂O₃ nanoparticles, thus leading to the PC-CPE.

The PC-CPE, due to the presence of safety reinforced PCE (providing ion transport channels) and also an elaborately structured ETPTA/ Al₂O₃ composite (acting as the mechanical framework), shows significant improvement in mechanical flexibility and high-temperature stability. Meanwhile, the PC-CPE precursor mixture (i.e., prior to UV curing) with well-tailored rheological properties, through collaboration with the UV-assisted imprint lithography (UV-IL) technique,^{26,42} produces the micro-patterned PC-CPE with tunable dimensions. Based on the structural and physicochemical characterization of the PC-CPE, its feasibility as a new solid-state electrolyte for flexible/safer batteries is explored by scrutinizing the charge/discharge behavior of cells, with a particular focus on cell performance under thermal shock condition (=130 °C/0.5 h).

3.2. Experimental

3.2.1. Fabrication of plastic crystal composite polymer electrolyte

SN, LiTFSI, ETPTA, and 2-hydroxy-2-methyl-1-phenyl-1-propanone (HMPP, photo-initiator) were purchased from Aldrich and Al₂O₃ nanoparticles (average powder size ~ 300 nm) were obtained from Sumitomo Chemical. The PCE was prepared by adding 1 M LiTFSI into SN melted at 60 °C.^{39,41} The weight based composition ratio of the PC-CPE precursor mixture was (ETPTA/PCE = 15/85 w/w)/ Al₂O₃ = 34/66 w/w, wherein the concentration of HMPP was fixed at 1.0 wt% of ETPTA. The precursor mixture was subjected to bead-milling for 0.5 h, in order to attain a uniform dispersion of Al₂O₃ nanoparticles. Subsequently, the precursor mixture was cast onto a polyethylene terephthalate (PET) sheet and then exposed to UV irradiation for 20 s, leading to the self-standing PC-CPE film. The UV curing was performed using a Hg UV-lamp (Lichtzen), with an irradiation peak intensity of approximately 2000 mW cm⁻² on the sample surface. The thickness of the resulting PC-CPE film was approximately 110 μm. PDMS stamps with microscale maze-patterns were obtained by thermally curing a commercially available liquid prepolymer mixture composed of a silicon elastomer base and a curing agent (Sylgard 184, Dow Corning) on a photoresist master at 80 °C for 5 h.²⁶ A schematic representation depicting the UV curing-assisted fabrication process, along with chemical structures and photographs depicting the mechanical bendability of the PC-CPE, is provided in Figure 10.

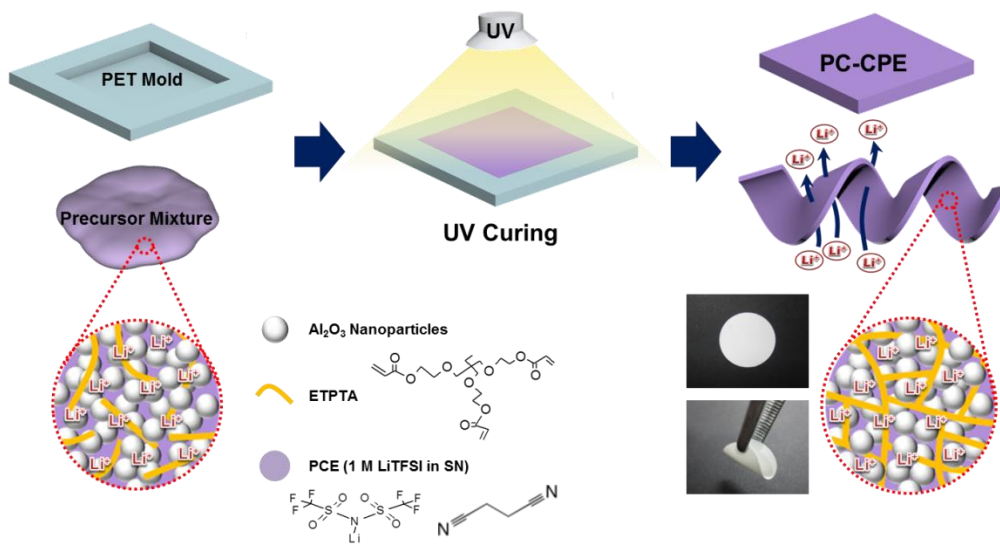


Figure 10. A schematic representation of UV curing-assisted fabrication process for PC-CPE, wherein chemical structures and photographs depicting mechanical bendability of PC-CPE are also depicted.

3.2.2. Characterization of microstructure, physical properties and electrochemical performance of plastic crystal composite polymer electrolyte

The thermal characteristics of the PC-CPE, particularly focusing on plastic crystal behavior of SN in the PC-CPE, were evaluated by differential scanning calorimetry (DSC, DuPont Q2000) at a heating rate of $20\text{ }^{\circ}\text{C min}^{-1}$. The UV curing reaction of the PC-CPE was examined using a FT-IR spectrometer (FT-3000, Excalibur) with a spectral resolution of 4 cm^{-1} . The morphology (in particular, dispersion state of Al_2O_3 nanoparticles) of the PC-CPE was investigated using a field emission scanning electron microscope (FE-SEM, S-4800, Hitachi). The mechanical bendability of the PC-CPE was estimated via a bending test using a universal tensile tester (LR 10K, Lloyd), where samples were subjected to repeated bending cycle (under longitudinal strain ranging from 10 to 30 mm) at a strain rate of 10 mm min^{-1} , where the number of bending cycles before breakdown of the samples represents their bendability.^{9,16,17} In addition, the mechanical deformability of the PC-CPE was further characterized after being wound around cylindrical glass rods (diameter = 2.5 and 5.0 mm). The maze-patterned PC-CPE was characterized with an optical microscope (BX41, Olympus), in addition to FE-SEM measurement. The viscosity of the PC-CPE precursor mixture was measured with a viscometer (Haake MARS 3, Thermo Electron GmbH). A conventional carbonate based liquid electrolyte (here, 1 M LiPF_6 in ethylene carbonate (EC)/dimethyl carbonate (DMC) = 1/1 v/v) was chosen as a control sample of the PC-CPE. The electrochemical stability window of the PC-CPE was measured by linear sweep voltammetry (LSV) performed on a working electrode of stainless-steel and a counter and reference electrode of lithium metal at a scan rate of 1.0 mV s^{-1} . The ionic conductivity of the PC-CPE was obtained using an impedance analyzer (VSP classic, Bio-Logic) over a frequency range of 1 to 10^6 Hz under a temperature range of 30 to $70\text{ }^{\circ}\text{C}$. To evaluate cell performance, a unit cell (2032 coin) was assembled by sandwiching the self-standing PC-CPE between the PCE-soaked LiCoO_2 cathode (LiCoO_2 (average particle size (D50) = 10 mm)/PVdF binder/Super-P = 95/3/2 w/w/w) and the PCE-soaked $\text{Li}_4\text{Ti}_5\text{O}_{12}$ anode ($\text{Li}_4\text{Ti}_5\text{O}_{12}$ (average particle size (D50) = 10 mm)/PVdF binder/Super-P = 88/10/2 w/w/w). A control cell was fabricated by assembling the same LiCoO_2 cathode and $\text{Li}_4\text{Ti}_5\text{O}_{12}$ anode with a polyethylene (PE) separator (thickness = 20 μm , Tonen), followed by being filled with the carbonate-based liquid electrolyte (1M LiPF_6 in EC/DMC = 1/1 v/v). The cells were cycled at a constant charge/discharge current density of 0.2 C ($=0.40\text{ mA cm}^{-2}$)/ 0.2 C under a voltage range of 1.5–2.7 V. The AC impedance of the cells was measured using the impedance analyzer over a frequency range from 10^{-3} to 10^6 Hz . To explore high-temperature stability of cells incorporating PC-CPE, aluminum (Al) pouch-type cells (width / length / thickness = 55 / 70 / 0.8 mm/mm/mm) were fabricated and subjected to a thermal shock test. After exposure to the thermal

shock condition (=130 °C/0.5 h), the charge/discharge behavior of cells was monitored at room temperature.

3.3. Results and discussion

3.3.1. Structural/electrochemical uniqueness of plastic crystal composite polymer electrolyte

The structural/electrochemical properties of PC-CPEs were characterized, with a focus on its plastic crystal behavior, chemical structure of the UV-cured ETPTA macromer and dispersion state of Al₂O₃ nanoparticles.

The DSC thermograms (Fig. 11(a)) show that two endothermic peaks assigned to characteristic transition temperatures of SN (T_{CP} (from crystalline to plastic phase) $\sim -39^{\circ}\text{C}$ and T_m (from plastic crystalline phase to melted state) $\sim 13^{\circ}\text{C}$)^{39,41} are observed in the PC-CPE. Comparison with the thermogram of PCE itself reveals no appreciable difference in the phase transition behavior, which indicates that the introduction of the UV-cured ETPTA/ Al₂O₃ framework does not disrupt the thermal characteristics of PCE. More details about plastic crystal behavior of PCE upon addition of lithium salts and variation of the polymer matrix were described in previous publications.^{9,16,39-41}

Another key component of the PC-CPE is the UV-cured ETPTA macromer. Fig. 11(b) exhibits that the characteristic FT-IR peaks assigned to acrylic C=C bonds^{26,41} of the ETPTA monomer disappeared after exposure to UV irradiation. This result demonstrates that the ETPTA monomer is photopolymerized under the presence of PCE and Al₂O₃ nanoparticles. In addition to this FT-IR result, the gel content (i.e., insoluble polymer fraction after solvent (DMC followed by acetone) extraction) of the PC-CPE was measured. Above 99% of gel by weight (here, Al₂O₃ nanoparticles are excluded)^{9,16} was observed, which is another evidence to confirm the successful UV curing reaction of the ETPTA monomer.

A cross-sectional FE-SEM image of the PC-CPE (Fig. 11(c)) shows that the Al₂O₃ nanoparticles are densely packed without serious agglomeration in the through-thickness direction. It is noteworthy that the highly reticulated nanoscale interstitial voids formed between the Al₂O₃ nanoparticles, corresponding to the space originally occupied with PCE that was removed using DMC (as an etching solvent) prior to the SEM measurement, represent the formation of well-networked ion-conductive pathways in the PC-CPE. The larger content of Al₂O₃ nanoparticles (Al₂O₃/(PCE + ETPTA) = 66/34 w/w) and their good compatibility with other components are expected to enable the development of such a unique porous morphology (i.e., highly-interconnected PCE phase in combination with the UV-cured ETPTA/ Al₂O₃ framework). The PCE-based, well-developed ion conductive channels in the PC-CPE are expected to play a crucial role in providing satisfactory level of cell performance, which will be further discussed in the following section.

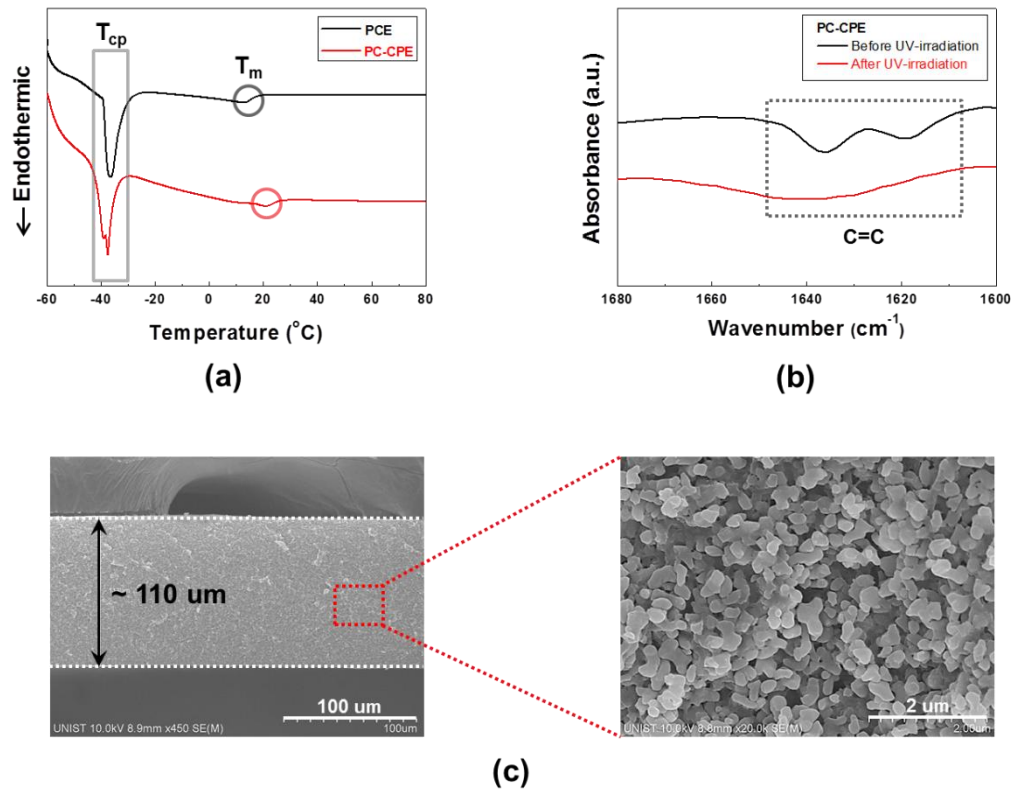
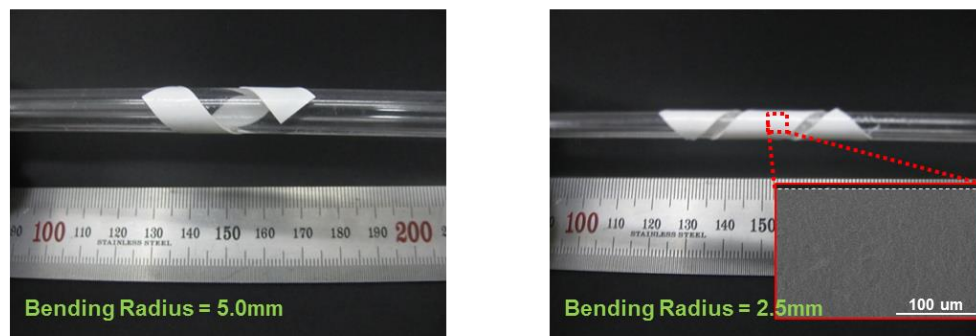


Figure 11. Structural characterization of PC-CPE: (a) DSC profiles showing characteristic transition temperatures (T_{cp} and T_m) of SN in PCE and PC-CPE; (b) FT-IR spectra (before/after UV curing) of acrylic C=C bonds ($1610 \sim 1625 \text{ cm}^{-1}$) of ETPTA in PC-CPE; (c) cross-sectional FE-SEM images of PC-CPE (thickness $\sim 110 \mu m$), wherein the high-magnification view exhibits the presence of highly-reticulated interstitial voids (that are originally occupied with PCE) formed between the Al_2O_3 nanoparticles.

The mechanical flexibility of the PC-CPE was quantitatively examined using a bending test (Fig. 12(a)). The PC-CPE shows strong resistance to mechanical rupture upon repeated bending cycle (under longitudinal strain ranging from 1 to 3 cm). Comparison with the result of a control sample incorporating no Al₂O₃ nanoparticles verifies that the UV-cured ETPTA/ Al₂O₃ framework effectively contributes to the mechanical bendability of the PC-CPE. While the control sample is broken down just after the 3rd bending cycle, the dimensional stability of the PC-CPE is preserved until the 45th bending cycle. This superior flexibility of the PC-CPE is ascribed to the presence of close-packed Al₂O₃ nanoparticles, which could serve as a mechanical buffer to mitigate stress localization occurring during the repeated bending cycle. It has already been reported that the advantageous effect of well-dispersed nanoparticles on the mechanical toughness of nanocomposites is mainly due to the creation of micro-voids that dissipate external stress.^{32,33} To further underline the excellent mechanical flexibility, the PCCPE was wound around a glass rod. Fig. 12(b) shows that no mechanical fracture is observed at the PC-CPE even after being wound around a narrow-diameter rod (= 2.5 and 5.0 mm). Moreover, neither micro-scale cracks nor physical defects were found in the PC-CPE (inset of Fig. 2(b)).



(a)



(b)

Figure 12. Mechanical flexibility of PC-CPE: (a) comparison of bendability between PC-CPE and control solid-state electrolyte incorporating no Al_2O_3 nanoparticles, wherein the samples are subjected to repeated bending cycle at a strain rate of 10 mm min^{-1} under longitudinal strain ranging from 1 to 3 cm; (b) photographs of PC-CPE after being wound along a glass rod (diameter = 2.5 and 5 mm), wherein the inset shows that neither micro-scale cracks nor physical defects are formed.

Another noteworthy achievement of the PC-CPE is the provision of a wide range of form factors. The PC-CPE precursor mixture (i.e., prior to UV-irradiation) exhibits unique rheological characteristics, in comparison to a conventional carbonate-based liquid electrolyte (here, 1 M LiPF₆ in EC/DMC = 1/1 v/v) showing low viscosity and Newtonian fluid behavior (Fig. 13). Specifically, the viscosity of the PC-CPE precursor mixture is substantially high and also decreases with increasing shear rate, representing a kind of shear-thinning behavior. Details on the rheological behavior of the electrolyte precursor mixture and its influence on the imprinting process were reported in the previous study.²⁶

A schematic illustration (Fig. 14(a)) depicts the UV-IL technique-driven micro-patterning procedure exploited herein, where pressing maze-patterned PDMS stamp onto the cast slurry of the PC-CPE precursor mixture and subsequent UV irradiation through the transparent PDMS stamp yield self-standing PC-CPE with replica of the maze-pattern. Fig. 14(b) shows an OM image of the PC-CPE precursor mixture before UV exposure, verifying the formation of the imprinted morphology with an inversely replicated maze pattern. Morphological characterization based on FE-SEM images (Fig. 14(c) and (d)) exhibits that the maze-patterned PC-CPE with finely-defined vertical edges is successfully formed, underlying the fabrication of the solid-state electrolyte with tunable dimensions down to micrometer scale. A high-magnification view (inset of Fig. 14(d)) demonstrates that Al₂O₃ nanoparticles are closely packed in the micro-patterned PC-CPE.

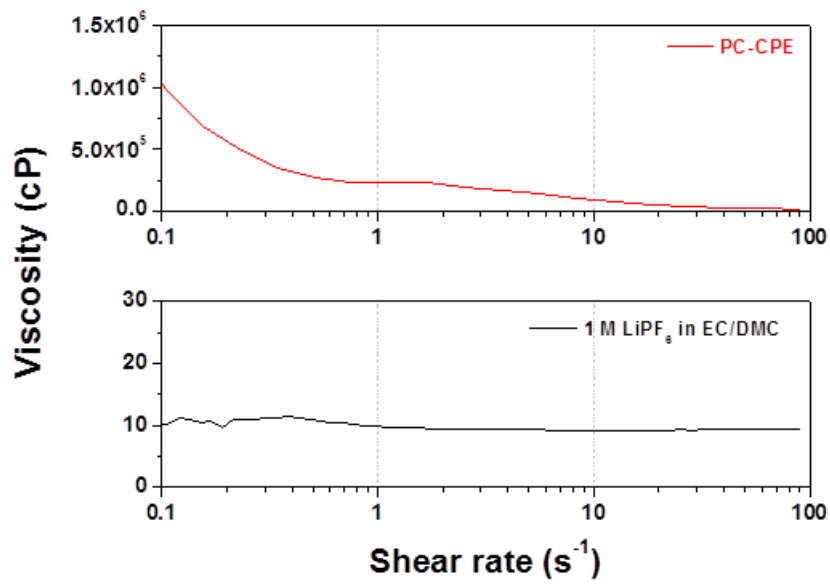


Figure 13. Rheological behavior of PC-CPE and carbonate-based liquid electrolyte (1M LiPF₆ in EC/DMC = 1/1 v/v), wherein viscosity is plotted as a function of shear rate.

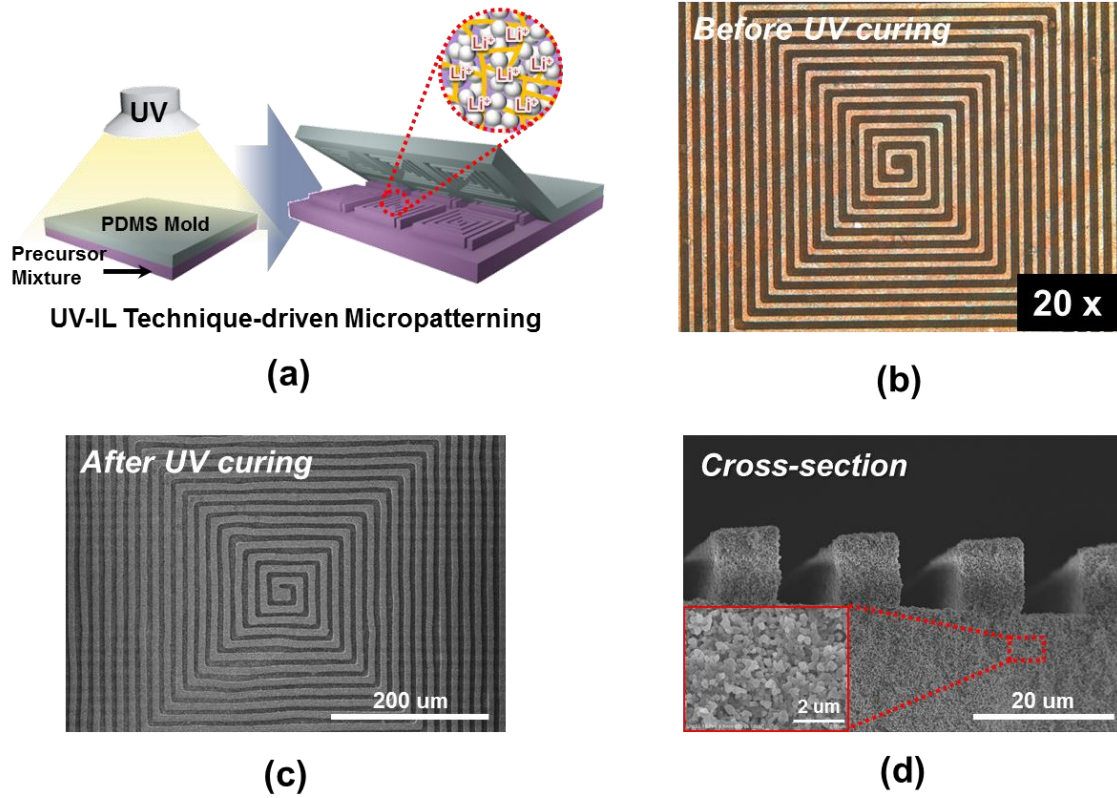


Figure 14. Structural characterization of maze-patterned PC-CPE: (a) a schematic illustration of UV-IL technique-driven micropatterning procedure; (b) OM image of PC-CPE precursor mixture prior to UV exposure; (c) FE-SEM image (top view) of microscale maze-patterned PC-CPE; (d) FE-SEM image (cross-sectional view) of microscale maze-patterned PC-CPE, wherein the inset shows that Al_2O_3 nanoparticles are closely packed in the micropatterned PC-CPE.

3.3.2. Electrochemical performance

The electrochemical performance of cells incorporating PC-CPE was characterized. It should be noted that the cell assembled with the PC-CPE does not incorporate a polyolefin separator membrane, implying that the PC-CPE acts as an electrolyte and also a separator membrane that keeps electrical isolation between electrodes.

The temperature-dependent ionic conductivity of the PC-CPE was measured and compared with that of the carbonate-based liquid electrolyte (1 M LiPF₆ in EC/DMC = 1/1 v/v) (Fig. 15). Although the ionic conductivity of the PC-CPE was found to be slightly lower than that of the carbonate-based liquid electrolyte, the PC-CPE delivers a satisfactory level of ionic conductivity (for example, $1.02 \times 10^{-3} \text{ S cm}^{-1}$ at room temperature), which is attributed to the well-interconnected ion-conductive channels in the PC-CPE (shown in Fig. 11(c)). Meanwhile, the electrochemical stability window of PC-CPE was estimated from LSV curves (Fig. 16). No electrochemical decomposition of any component in the PC-CPE takes place below 5.0 V vs. Li⁺/Li, indicating potential application to high-voltage batteries. In addition, owing to the UV-cured ETPTA/Al₂O₃ framework, the PC-CPE shows the slight improvement in the anodic stability compared to the PCE. Further analysis of the electrochemical stability of the PC-CPE will be conducted in future studies.

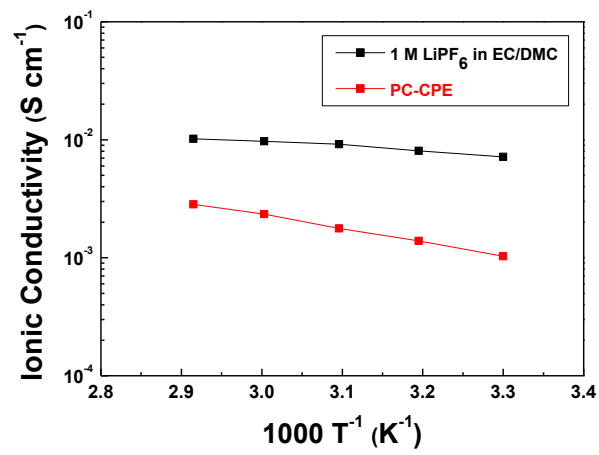


Figure 15. Temperature-dependent ionic conductivity (temperature range = 30 - 70 °C) of PC-CPE and carbonate-based liquid electrolyte (1M LiPF₆ in EC/DMC = 1/1 v/v).

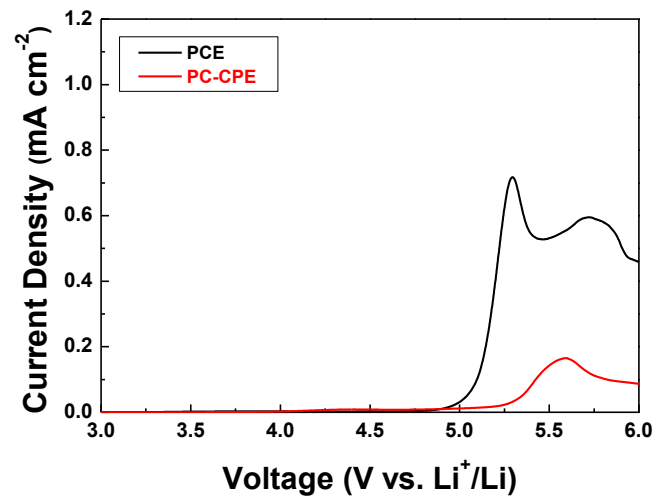


Figure 16. Linear sweep voltammograms (LSV) of PC-CPE at a scan rate of 1.0 mV s⁻¹.

3.3.3. Cell performance

Fig. 17 shows charge/discharge profiles of cells as a function of cycle number at a constant charge/discharge current density ($= 0.2 \text{ C}/0.2 \text{ C}$) under a voltage range of 1.5–2.7 V. Here, a cell incorporating the carbonate-based liquid electrolyte (1 M LiPF_6 in EC/DMC = 1/1 v/v) and a PE separator was compared as a control system. The cell assembled with the PC-CPE presents an initial discharge capacity of 123 mA h g^{-1} and also stable charge/discharge behavior up to the 40th cycle, although the capacity retention ($= 96.9\%$) appears to be slightly lower than that ($= 99.6\%$) of the control cell. This good cycling performance of the PC-CPE was verified by analyzing the AC impedance spectra of cells after the 1st and the 40th cycle (Fig. 18). The increase in cell impedance during the cycling is found to be negligibly small ($Z_{\text{Re}}(40\text{th cycle}) - Z_{\text{Re}}(1\text{st cycle}) = \Delta Z_{\text{Re}} < 10 \text{ ohm}$).

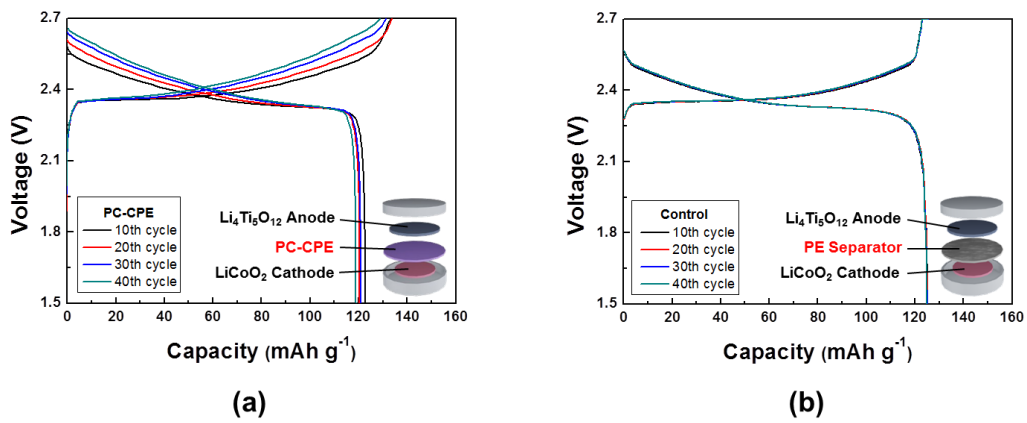


Figure 17. Charge/discharge profiles of coin-type full cells as a function of cycle number, wherein the cells are cycled at a constant charge/discharge current density of 0.2 C (= 0.40 mA cm⁻²)/0.2 C under a voltage range of 1.5 - 2.7 V: (a) LiCoO₂/PC-CPE/Li₄Ti₅O₁₂; (b) LiCoO₂/PE separator/Li₄Ti₅O₁₂.

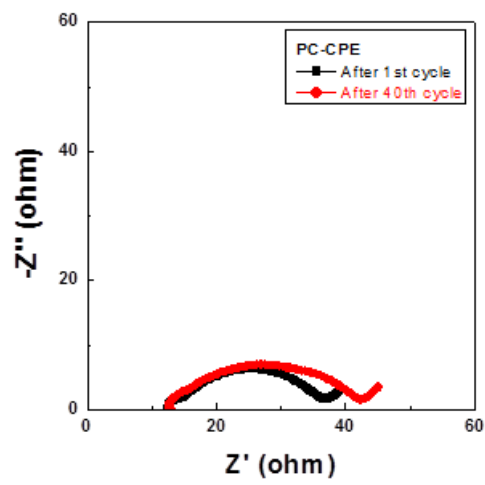


Figure 18. Variation in AC impedance spectra ($1^{\text{st}} \rightarrow 40^{\text{th}}$ cycle) of cells assembled with PC-CPE.

3.3.4. Thermal stability

To elucidate the effect of PC-CPE on the thermal stability of a cell, Al pouch-type cells were fabricated. The cells were subjected to the thermal shock condition (= 130 °C/0.5 h) and then their cell performance was monitored at room temperature. Fig. 19(a) shows that the control cell assembled with the carbonate-based electrolyte and the PE separator loses its electrochemical activity after exposure to the thermal shock. Specifically, the cell voltage is down to 0 V and does not return to an initial charge state, indicating the occurrence of internal short-circuit between the anode and the cathode. This internal short-circuit failure may result from thermal shrinkage of the PE separator and also the presence of a volatile carbonate-based electrolyte. In contrast, the cell incorporating the PC-CPE shows stable charge/discharge profiles after the thermal shock. This superior thermal stability of the PC-CPE was further confirmed by observing the inappreciable growth in cell impedance (Fig. 20). Fig. 19(b) summarizes the variation in discharge capacity and charge voltage (inset of Fig. 19(b)) of the cells before/after the thermal shock.

To attain in-depth understanding of the influence of separators on internal short-circuit failure of cells, dimensional change of the PC-CPE and the PE separator was examined after exposure to the same thermal shock condition (Fig. 19(c)). The area-based dimensional shrinkage (ΔA) of the PC-CPE was found to be negligibly small, as compared to the PE separator ($\Delta A \sim 43\%$). This result demonstrates that the PC-CPE could act as a self-standing solid-state electrolyte outperforming the PE separator membrane in terms of thermal shrinkage. Commercial PE separators are known to suffer from large thermal shrinkage upon exposure to high-temperature, because of their low melting temperature (below 140 °C) and stretching process essentially used for separator manufacturing.^{36,43} This poor thermal stability of PE separators is considered as a major cause of the internal short-circuit failures. Meanwhile, the ionic conductivity of the PC-CPE was compared before/after the same thermal shock (Fig. 19(d)). No decrease in the ionic conductivity was observed, demonstrating the excellent thermal tolerance of the PC-CPE.

As another piece of evidence to prove the superior thermal stability of the PC-CPE, the change in cell dimension after the thermal shock test was examined. Fig. 21(a) shows that the cell incorporating the PC-CPE remains intact without dimensional distortion, in comparison to the control cell that was greatly swollen up. The dynamic mode TGA measurement (Fig. 21(b)) of the PC-CPE and carbonate-based electrolyte delivers meaningful data to explain this intriguing behavior of cell swelling. Negligible loss in weight was observed at the PC-CPE up to approximately 130 °C, verifying the excellent thermal stability of the PC-CPE. On the other hand, the carbonate-based electrolyte shows the rapid weight loss mainly due to the presence of volatile DMC component (boiling temperature ~ 90 °C).^{20,44}

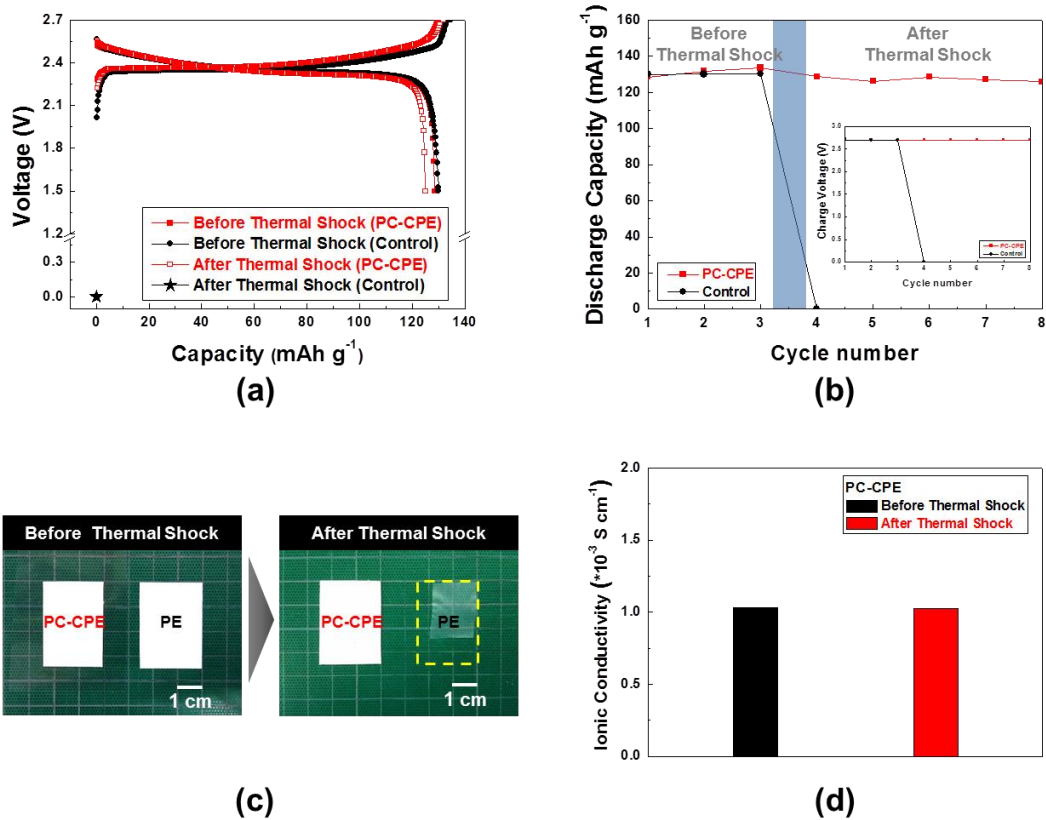


Figure 19. Thermal stability of Al pouch-type full cells assembled with PC-CPE or carbonate-based liquid electrolyte (1M LiPF₆ in EC/DMC = 1/1 v/v) and PE separator: (a) variation in charge/discharge profiles of cells after exposure to thermal shock (= 130 °C/0.5 h); (b) variation in discharge capacity and charge voltage (inset) of cells before/after the thermal shock. (c) Comparison of thermal shrinkage between PC-CPE and PE separator after exposure to the thermal shock. (d) Ionic conductivity of PC-CPE before/after the thermal shock.

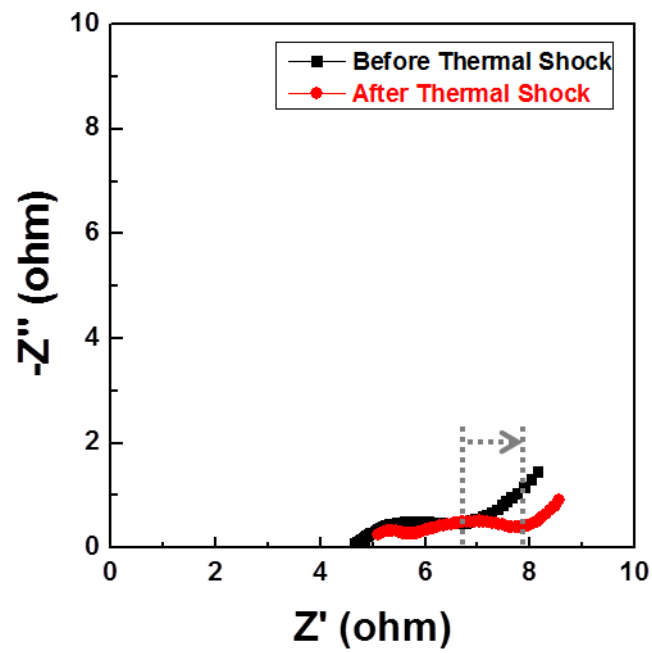
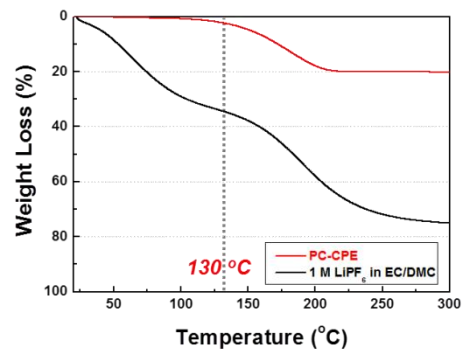


Figure 20. Variation in AC impedance spectra of cells assembled with PC-CPE after exposure to thermal shock (= 130°C/0.5 h).



(a)



(b)

Figure 21. (a) Photographs showing the swelling behavior of cells assembled with PC-CPE or carbonate-based liquid electrolyte (1M LiPF₆ in EC/DMC = 1/1 v/v), after exposure to thermal shock (= 130°C/0.5 h). (b) Dynamic mode TGA profiles of PC-CPE and carbonate-based electrolyte (1M LiPF₆ in EC/DMC = 1/1 v/v).

3.4. Conclusion

The PC-CPE is a new class of shape-deformable and safety reinforced solid-state electrolyte for flexible/ safer lithium-ion batteries. The in-depth structural characterization indicated that the PCE was successfully combined with the UV-cured ETPTA macromer/close-packed Al_2O_3 nanoparticle framework, leading to the PC-CPE. In comparison to the conventional carbonate-based liquid electrolyte, the PC-CPE provided the notable improvement in mechanical properties and thermal stability. The PC-CPE precursor mixture with well-tailored rheological characteristics, in collaboration with the UV-IL process, allowed the development of the PC-CPE featuring microscale maze-pattern. Even after exposure to the thermal shock (= $130^\circ\text{C}/0.5$ h), the cell incorporating the PC-CPE delivered the stable charge/discharge behavior without suffering from safety issues such as cell swelling and internal short-circuit failure. We believe that the material/structure concept used for fabrication of PC-CPE is simple and versatile, which thus can be readily applicable to a wide variety of next-generation flexible energy storage systems as a platform strategy enabling advanced solid-state electrolytes.

Reference

- 1 Tarascon, J. M. & Armand, M. Issues and challenges facing rechargeable lithium batteries. *Nature* **414**, 359-367 (2001).
- 2 Gates, B. D. Flexible electronics. *Science* **323**, 1566-1567 (2009).
- 3 Rogers, J. A., Someya, T. & Huang, Y. Materials and mechanics for stretchable electronics. *Science* **327**, 1603-1607 (2010).
- 4 Zhou, G., Li, F. & Cheng, H.-M. Progress in flexible lithium batteries and future prospects. *Energy & Environmental Science* **7**, 1307-1338 (2014).
- 5 Li, L., Wu, Z., Yuan, S. & Zhang, X.-B. Advances and challenges for flexible energy storage and conversion devices and systems. *Energy & Environmental Science* (2014).
- 6 Wang, X. *et al.* Flexible Energy-Storage Devices: Design Consideration and Recent Progress. *Advanced Materials* **26**, 4763-4782 (2014).
- 7 Lee, Y.-H. *et al.* Wearable Textile Battery Rechargeable by Solar Energy. *Nano letters* **13**, 5753-5761 (2013).
- 8 Ren, J. *et al.* Elastic and Wearable Wire-Shaped Lithium-Ion Battery with High Electrochemical Performance. *Angewandte Chemie* (2014).
- 9 Choi, K. H. *et al.* Thin, Deformable, and Safety-Reinforced Plastic Crystal Polymer Electrolytes for High-Performance Flexible Lithium-Ion Batteries. *Advanced Functional Materials* **24**, 44-52 (2014).
- 10 Lee, S.-Y. *et al.* Progress in flexible energy storage and conversion systems, with a focus on cable-type lithium-ion batteries. *Energy & Environmental Science* **6**, 2414-2423 (2013).
- 11 Hu, L. *et al.* Stretchable, porous, and conductive energy textiles. *Nano letters* **10**, 708-714 (2010).
- 12 Hu, L., Wu, H., La Mantia, F., Yang, Y. & Cui, Y. Thin, flexible secondary Li-ion paper batteries. *Acs Nano* **4**, 5843-5848 (2010).
- 13 Kaempgen, M., Chan, C. K., Ma, J., Cui, Y. & Gruner, G. Printable thin film supercapacitors using single-walled carbon nanotubes. *Nano letters* **9**, 1872-1876 (2009).
- 14 Jost, K. *et al.* Carbon coated textiles for flexible energy storage. *Energy & Environmental Science* **4**, 5060-5067 (2011).
- 15 Weng, W. *et al.* Winding Aligned Carbon Nanotube Composite Yarns into Coaxial Fiber Full Batteries with High Performances. *Nano letters* (2014).
- 16 Ha, H.-J. *et al.* UV-curable semi-interpenetrating polymer network-integrated, highly bendable plastic crystal composite electrolytes for shape-conformable all-solid-state lithium ion batteries. *Energy & Environmental Science* **5**, 6491-6499 (2012).
- 17 Kim, S.-H., Choi, K.-H., Cho, S.-J., Kil, E.-H. & Lee, S.-Y. Mechanically compliant and

- lithium dendrite growth-suppressing composite polymer electrolytes for flexible lithium-ion batteries. *Journal of Materials Chemistry A* **1**, 4949-4955 (2013).
- 18 Li, H., Wang, Z., Chen, L. & Huang, X. Research on Advanced Materials for Li-ion Batteries. *Advanced Materials* **21**, 4593-4607 (2009).
- 19 Palacín, M. R. Recent advances in rechargeable battery materials: a chemist's perspective. *Chemical Society Reviews* **38**, 2565-2575 (2009).
- 20 Quartarone, E. & Mustarelli, P. Electrolytes for solid-state lithium rechargeable batteries: recent advances and perspectives. *Chemical Society Reviews* **40**, 2525-2540 (2011).
- 21 Lee, S. Y., Meyer, W. H. & Wegner, G. Phase Behavior of Gel-Type Polymer Electrolytes and Its Influence on Electrochemical Properties. *ChemPhysChem* **6**, 49-53 (2005).
- 22 Hassoun, J., Panero, S., Reale, P. & Scrosati, B. A New, Safe, High-Rate and High-Energy Polymer Lithium-Ion Battery. *Advanced Materials* **21**, 4807-4810 (2009).
- 23 Kil, E. H., Ha, H. J. & Lee, S. Y. A Facile Approach to Fabricate Self-Standing Gel-Polymer Electrolytes for Flexible Lithium-Ion Batteries by Exploitation of UV-Cured Trivalent/Monovalent Acrylate Polymer Matrices. *Macromolecular Chemistry and Physics* **212**, 2217-2223 (2011).
- 24 Ha, H.-J., Kwon, Y. H., Kim, J. Y. & Lee, S.-Y. A self-standing, UV-cured polymer networks-reinforced plastic crystal composite electrolyte for a lithium-ion battery. *Electrochimica Acta* **57**, 40-45 (2011).
- 25 Kim, S. H. *et al.* Optofluidic assembly of colloidal photonic crystals with controlled sizes, shapes, and structures. *Advanced Materials* **20**, 1649-1655 (2008).
- 26 Kil, E. H. *et al.* Imprintable, Bendable, and Shape-Conformable Polymer Electrolytes for Versatile-Shaped Lithium-Ion Batteries. *Advanced Materials* **25**, 1395-1400 (2013).
- 27 Gerbaldi, C. *et al.* UV-cured polymer electrolytes encompassing hydrophobic room temperature ionic liquid for lithium batteries. *Journal of Power Sources* **195**, 1706-1713 (2010).
- 28 Liu, S. *et al.* Effect of nano-silica filler in polymer electrolyte on Li dendrite formation in Li/poly (ethylene oxide)-Li (CF₃SO₂)₂N/Li. *Journal of Power Sources* **195**, 6847-6853 (2010).
- 29 Park, H. E., Hong, C. H. & Yoon, W. Y. The effect of internal resistance on dendritic growth on lithium metal electrodes in the lithium secondary batteries. *Journal of Power Sources* **178**, 765-768 (2008).
- 30 Rosso, M. *et al.* Dendrite short-circuit and fuse effect on Li/polymer/Li cells. *Electrochimica acta* **51**, 5334-5340 (2006).
- 31 Lauke, B. On the effect of particle size on fracture toughness of polymer composites.

- Composites Science and Technology* **68**, 3365-3372 (2008).
- 32 Cotterell, B., Chia, J. & Hbaieb, K. Fracture mechanisms and fracture toughness in semicrystalline polymer nanocomposites. *Engineering Fracture Mechanics* **74**, 1054-1078 (2007).
- 33 Meijer, H. E. & Govaert, L. E. Mechanical performance of polymer systems: the relation between structure and properties. *Progress in polymer science* **30**, 915-938 (2005).
- 34 Doyle, M., Newman, J., Gozdz, A. S., Schmutz, C. N. & Tarascon, J. M. Comparison of modeling predictions with experimental data from plastic lithium ion cells. *Journal of the Electrochemical Society* **143**, 1890-1903 (1996).
- 35 Abraham, K. Directions in secondary lithium battery research and development. *Electrochimica Acta* **38**, 1233-1248 (1993).
- 36 Choi, E.-S. & Lee, S.-Y. Particle size-dependent, tunable porous structure of a SiO₂/poly (vinylidene fluoride-hexafluoropropylene)-coated poly (ethylene terephthalate) nonwoven composite separator for a lithium-ion battery. *Journal of Materials Chemistry* **21**, 14747-14754 (2011).
- 37 Liao, Y. *et al.* Fumed silica-doped poly (butyl methacrylate-styrene)-based gel polymer electrolyte for lithium ion battery. *Journal of Membrane Science* **352**, 95-99 (2010).
- 38 Li, Z., Su, G., Wang, X. & Gao, D. Micro-porous P (VDF-HFP)-based polymer electrolyte filled with Al₂O₃ nanoparticles. *Solid State Ionics* **176**, 1903-1908 (2005).
- 39 Das, S., Prathapa, S. J., Menezes, P. V., Row, T. N. G. & Bhattacharyya, A. J. Study of ion transport in lithium perchlorate-succinonitrile plastic crystalline electrolyte via ionic conductivity and in situ cryo-crystallography. *The Journal of Physical Chemistry B* **113**, 5025-5031 (2009).
- 40 Fan, L. Z., Hu, Y. S., Bhattacharyya, A. J. & Maier, J. Succinonitrile as a versatile additive for polymer electrolytes. *Advanced Functional Materials* **17**, 2800-2807 (2007).
- 41 Alarco, P.-J., Abu-Lebdeh, Y., Abouimrane, A. & Armand, M. The plastic-crystalline phase of succinonitrile as a universal matrix for solid-state ionic conductors. *Nature materials* **3**, 476-481 (2004).
- 42 Yao, J. *et al.* Soft embossing of nanoscale optical and plasmonic structures in glass. *ACS nano* **5**, 5763-5774 (2011).
- 43 Arora, P. & Zhang, Z. Battery separators. *Chemical reviews* **104**, 4419-4462 (2004).
- 44 Xu, K. Nonaqueous liquid electrolytes for lithium-based rechargeable batteries. *Chemical reviews* **104**, 4303-4418 (2004).